MODELING OF SURFACE MICROTOPOGRAPHY AND ITS IMPACTS ON HYDROLOGIC PROCESSES

A Thesis
Submitted to the Graduate Faculty
of the
North Dakota State University
of Agriculture and Applied Science

By

Noah Lebassi Habtezion

In Partial Fulfillment of the Requirements
for the Degree of
MASTER OF SCIENCE

Major Department:
Civil and Environmental Engineering

November 2014

Fargo, North Dakota

North Dakota State University
Graduate School

Title

Modeling of Surface Microtopography and Its Impacts on Hydrologic Processes

By

Noah Lebassi Habtezion

The Supervisory Committee certifies that this ***disquisition*** complies with North Dakota State University's regulations and meets the accepted standards for the degree of

MASTER OF SCIENCE

SUPERVISORY COMMITTEE:

Dr. Xuefeng Chu
Chair

Dr. Zhulu Lin

Dr. Frank Casey

Dr. Xiangfa Wu

Approved:

11/7/2014	Dr. Dinesh Katti
Date	Department Chair

ABSTRACT

Understanding the impacts of surface microtopography on hydrologic processes is critical. The objectives of this thesis research are: (1) to evaluate the effects of DEM resolution on microtopographic characteristics, hydrologic connectivity, and modeling of hydrologic processes; and (2) to assess the influences of multiple rainfall events on surface and subsurface hydrologic processes with the use of a puddle-to-puddle (P2P) modeling system. The change in DEM resolution has a significant effect on how surface microtopography is depicted, which in turn alters the hydrologic response of a topographic surface. The smoothing of reduced DEM resolution tends to enhance hydrologic connectivity, reduce the depression storage and infiltration, and increase surface runoff. Temporal rainfall distribution results in spatio-temporal variations in soil water dynamics, depression storage, infiltration, hydrologic connectivity, and surface runoff. The reduction in ponding time and infiltration, and the enhancement of hydrologic connectivity further caused earlier and greater surface runoff generation.

ACKNOWLEDGEMENTS

First, I am highly indebted to my advisor, Dr. Xuefeng Chu for giving me the opportunity to be his graduate student and allowing me to conduct independent and high impact research. During my stay at NDSU, I learned a lot from him and his continued professional support, guidance, and encouragement were tremendous. I would like to gratefully acknowledge the financial support from the National Science Foundation (NSF, Grant No. EAR-0907588), North Dakota Water Resources Research Institute (NDWRRI), and the Department of Civil and Environmental Engineering, without which this thesis research would not have been possible.

I would like to extend my gratitude to the other committee members: Dr. Zhulu Lin, Dr. Frank Casey, and Dr. Xiangfa Wu for their time, willingness to serve, and providing professional input and suggestions. Thanks also to my colleagues, Dr. Jun Yang, Dan Bogart, Yingjie Yang, Yaping Chi, and Yang Liu for their encouragement and contribution to the group research.

Finally, thanks are due to my beloved parents, my father, Lebassi Habtezion and my mother, Lemlem Embaye, and my siblings for their everlasting love, support, and encouragement. They have always been my source of inspiration and motivation. I would also like to thank all family and friends for their encouragement and assistance. Special thanks go to my friends in Fargo, ND.

TABLE OF CONTENTS

LIST OF TABLES

LIST OF FIGURES

LIST OF ABBREVIATIONS

ACs ..... Connected Areas

C2C ..... Cell to Cell

DEM ..... Digital Elevation Model

LiDAR ..... Light Detection And Ranging

MDS ..... Maximum Depression Storage

MPA ..... Maximum Ponding Area

NCA ..... Number of Connected Areas

NLCA ..... Normalized Connected Area

OBIA ..... Object Based Image Analysis

P2P ..... Puddle-to-Puddle

PAs ..... Ponding Areas

PBU ..... Puddle Based Unit

PD ..... Puddle Delineation

RGB ..... Red, Green, and Blue

CHAPTER 1. GENERAL INTRODUCTION

Understanding the impacts of surface microtopography on hydrologic processes is critical. In order to improve hydrologic modeling, accurate surface topographic information is needed as the hydrologic processes basically reflect the responses of the topographic surface. One of the important variables that may be used in characterization of a topographic surface is elevation. Soil roughness elements quantify the variation in surface elevation and are available at different scales. Roughness elements include grains, aggregates, clods, tillage marks, and landscape features (Huang and Bradford 1992). Surface microtopography is a small scale surface roughness that plays a pivotal role in surface and subsurface hydrology and is portrayed by using various topographic features such as depressions/puddles, peaks, ridges, and channels (Chu 2011). Furthermore, the study of surface microtopography is essential for watershed modeling and management. Although it is not quantified precisely in most of the existing hydrologic models, surface microtopography must be well defined and outlined (Chu et al. 2010). When rain falls on a surface, the water first infiltrates into soil. After a ponding condition is achieved, filling of surface depressions starts. After depressions are fully filled, water may spill to the downstream or to adjacent depressions so that merged puddles may be formed. Combined puddles might separate during drying to form independent puddles. This dynamic puddle-to-puddle filling-spilling-merging-splitting process is referred to as the P2P process (Chu 2011). The study of microdepressions is important as the functions of such surface topographic features may go beyond surface water detention and alter drainage flow paths and the inception of overland flow (Darboux et al. 2001). In addition, they may affect the quantification of depression storage (Huang and Bradford 1990), partitioning of rainfall into infiltration and surface runoff, and the whole water mass balance of a hydrologic system (Chu 2011). Moreover, the spatio-

temporal distributions and depths of runoff water are functions of surface topography (Huang and Bradford 1990). To improve the understanding of surface runoff and infiltration processes, it is necessary to investigate surface microtopography and depressions storage. Surface microtopography is basically composed of small features. As surface depression storage depth has a comparable magnitude to these microtopographic features, quantifying the spatial surface microtopography becomes imperative as opposed to using single length scale (Huang and Bradford 1990). Use of a single scale can smooth several microtopographic features and ultimately underestimate the surface depression storage.

Quantifying the effects and interrelationships of different hydrologic variables and processes has been presenting perplexing challenges to surface microtopography characterization and hydrologic modeling. Resolution of a digital elevation model (DEM) and temporal distribution of rainfall are two factors that have a great impact on both surface microtopographic and hydrologic modeling. Grid spacing (i.e., DEM resolution) determines the extent of microtopographic information to be revealed or hidden. At larger grid spacing, some topographic features may be hidden and aggregated together, while at a finer scale (higher resolution), the topographic details can resemble the topography of a real surface. This effect can change the virtual hydrologic response of the topographic surface drastically. Temporal rainfall distribution is another important factor that can amend the dynamics of hydrologic processes over a topographic surface. When rain falls on a topographic surface, the water will infiltrate until the rainfall intensity exceeds the infiltration capacity. Thereafter, water will start to pond on the surface. When rainfall ceases, the surface will start drying and the ponded water will be depleted. During the pre-ponding, post-ponding and the dry time periods, soil moisture changes in different ways. Consequently, when another rainfall event starts, due to the change in moisture

regime of the topographic surface, hydrologic processes often show dissimilar behaviors when compared with those in the preceding rainfall event. Generally, DEM resolution and multiple rainfall events can affect the surface microtopographic characteristics, quantification of surface depression storage, hydrologic connectivity, spatio-temporal distribution of infiltration, overland flow generation processes, and subsurface water dynamics. Hence, a thorough study of such factors becomes important and their consideration can ameliorate the accuracy of currently used hydrologic models and improve the existing modeling approaches.

1.1. Topographic Surface Characterization

Topographic surface data can be acquired in several ways (Schiewe 2002; MacMillan et al. 2003). DEMs and images have been some of the widely used data sources. Due to the scale of microtopographic study, precise instruments that can collect data in smaller units have been needed. Moreover, due to the lack of fast data processing machines, studies that focused on microtopography were facing limitations (e.g., Darboux et al. 2001). Technological advancements enabled researchers to examine microtopography and other related hydrologic processes at an increasingly smaller scale. Laser scanners brought major breakthrough in microtopographic studies (Govers 2000). Scanners which can acquire data in a resolution less than a millimeter are in common use for DEMs. Darboux and Huang (2003) developed an instantaneous-profile laser scanner, which was able to capture small scale data at a faster rate. Similarly, images were successfully utilized in topographic surface characterization and analysis (Blaschke 2010; Drăguţ and Eisank 2012). Depending on the techniques and types of data acquired, several methods have been proposed for topographic surface characterization and analysis. Deterministic approach might be employed to extract information from DEM data. While for images, some statistical approaches might be necessary to get accurate results.

In this thesis research, an Object-Based Image Segmentation (OBIS) tool and a Surface Topographic Parameters (STP) tool have been developed for characterization of surface microtopography and computation of topographic parameters. In addition, the Puddle Delineation (PD) program (Chu et al. 2010) was used for puddle characterization and modeling. It is also an essential part of the P2P modeling system.

1.1.1. Object-based image analysis

Object-based image analysis (OBIA) is a powerful method, by which similar pixels surrounding a given point are conglomerated to form an object, instead of treating pixels individually. Due to the lack of high resolution images, pixel-based image analysis was the only option available. The advancement in remote sensing has dramatically improved image quality and, on the other hand, created a challenge that is difficult to overcome with the classical pixel-based image analysis. Using the latest imaging technologies, obtaining high resolution images is not difficult. Hence, instead of trying to analyze pixels individually, considering groups of pixels became an alternative and probably the efficient way with considerable advantages. This method is being utilized in a wide range of engineering and other fields.

An object-based image segmentation (OBIS) tool has been developed based on the concept of OBIA in this study. K-means algorithm, color frequency table, and Euclidean distance were combined in order to avoid human intervention and come up with a non-supervised clustering approach. K-means is one of the simplest, fastest and efficient non-hierarchical clustering algorithms. In a set of T data points $p_1, p_2, p_3, \ldots, p_T$; K clusters $U_1, U_2, U_3, \ldots, U_K$; and K corresponding cluster centers $u_1, u_2, u_3, \ldots, u_K$ [note that each cluster contains t_i data points $(0 < t_i < T)$], the mean-square-error function is given by (Zalik 2008):

$$E = \sum_{i=1}^{i=K} \sum_{p_i \in U_i} \left\| p_i - u_i \right\|^2 \qquad (1.1)$$

The idea behind the K-means clustering algorithm is to minimize the error function E so that the data point p_i will be assigned to the cluster U_i with the minimum E. The cluster center shifts position adaptively and the iteration will terminate when the cluster center ceases to move and stays at the centroid of the cluster. The parameters that need to be specified are the number of clusters, their seeding location and threshold between clusters. Once these are specified, each data point (pixel) is assigned to a cluster center based on the minimized error function criteria. Based on this, a new cluster center is calculated and this process is repeated until the calculated cluster center is identical to the previous one. And this would be the final stage of the clustering, and the image would be segmented into a number of objects. The number of the objects is equal to the number of clusters specified.

K-means is most commonly used with Euclidean distance when the distance between the image data points (pixels) and the cluster centers is calculated (Jain 2010). Color is defined by three positive primary color values which are Red (R), Green (G), and Blue (B), indicating that the color space is the representation of the primary colors (R, G, and B) in a space Cartesian coordinate system as a volume (Wright 2007). Therefore, vector addition should be used when calculating the Euclidean distance between two color points. In a set of T data points $p_1, p_2, p_3, \ldots, p_T$; K clusters $U_1, U_2, U_3, \ldots, U_K$ and K corresponding cluster centers $u_1, u_2, u_3, \ldots, u_K$, the Euclidean distance between the first cluster center and any data point can be calculated by:

$$d_{1i} = \sqrt{(u_{1R} - p_{iR})^2 + (u_{1G} - p_{iG})^2 + (u_{1B} - p_{iB})^2} \quad (1 \le i \le T) \tag{1.2}$$

1.1.2. OBIS tool

The Windows-based OBIS tool (Figure 1.1) was developed using C#. In the OBIS program, the K-means algorithm along with a RGB color frequency table is used for image segmentation. Specifically, the number of clusters and threshold are specified for an image. The

image is then segmented into a number of homogeneous regions determined by the clusters. The color frequency table lists the number of times that each color is used in the image (i.e., color-frequency distribution). It is important to know where the initial cluster centers are located (seeding) as the entire process is very sensitive to this initialization criteria. If the cluster centers did not fall on the right locations, the segmentation process may end up with unexpected results. In OBIS, instead of randomly seeding initial cluster centers, they are made to fall on the predetermined color frequency table top list colors. Subsequent cluster centers are selected starting from top in such a way to exceed the specified threshold. This dramatically improves the traditional K-means clustering as it minimizes the sensitivity to initialization criteria and makes it more predictable and sensible.

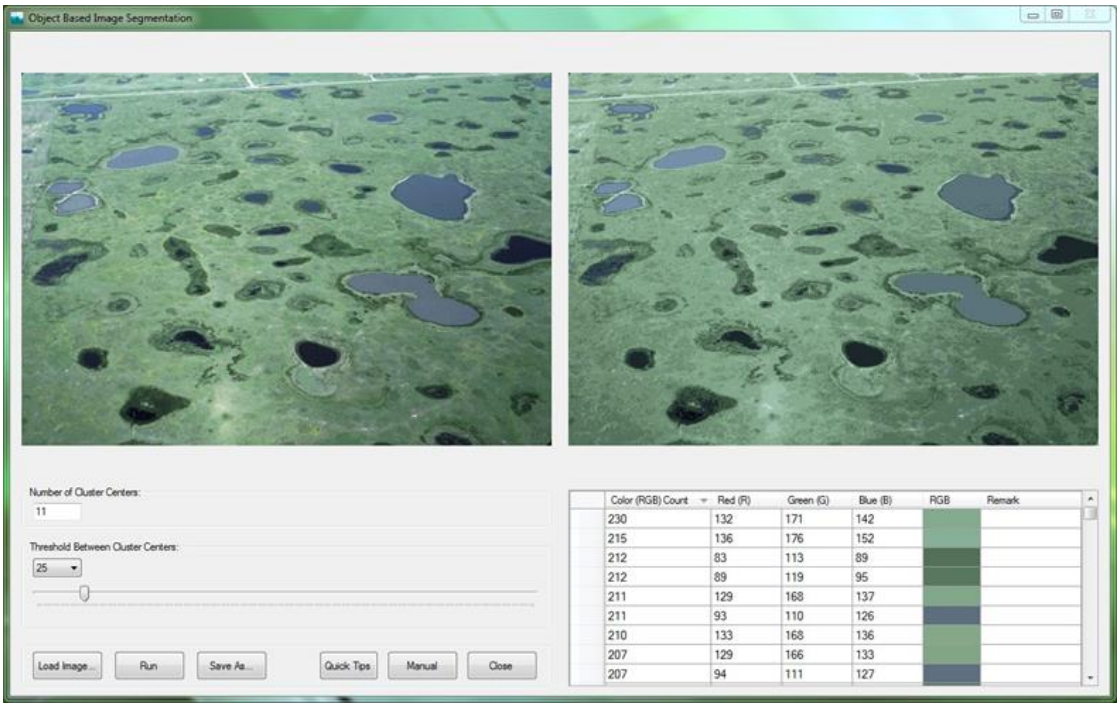

Figure 1.1. Main interface of OBIS tool

1.1.3. Surface topographic parameters

The availability of high-resolution DEM data allows one to accurately characterize surface topography, which further improves watershed delineation and the related hydrologic and environmental modeling. Quantitative DEM-based analyses provide essential hydrotopographic information. The commonly used surface topographic metrics include slope, aspect, profile curvature, plan curvature, tangential curvature, and mean curvature. The equations used to calculate each parameter and the kernel window used in their derivation are given below.

Kernel window

A kernel or moving window was used to calculate topographic parameters for each DEM grid. The size of the kernel window was 3 × 3 (Figure 1.2). "z" denotes the grid elevation. Numbering starts from the upper left corner of the kernel window. The central cell is "the cell in focus." Assuming that there exists a function to represent the topographic land surface: z = h(x,y), the first and second derivatives of h(x,y) can then be calculated based on the nine cells.

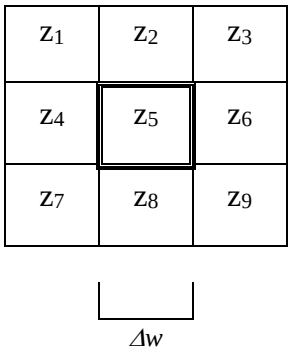

Figure 1.2. 3 × 3 kernel window with a cell size of Δw

Slope (S)

Slope gradient is given by Evans-Young method (Pennock et al. 1987; Pike at al. 2008):

$$S = 100\sqrt{m^2 + n^2} \tag{1.3}$$

where S = slope (%); $m = \partial z / \partial x$; $n = \partial z / \partial y$; z = elevation; and x, y = coordinates.

Aspect (A)

Aspect can be expressed as (Shary et al. 2002; Olaya 2008):

$$A = -90(1 - sign(n)) \cdot (1 - |sign(m)|) + 180(1 + sign(m)) - \frac{180}{\pi} \cdot sign(m) \arccos\left(\frac{-n}{\sqrt{m^2 + n^2}}\right) \quad (1.4)$$

$$\begin{cases} sign(n), sign(m) = 1 & n, m > 0 \\ sign(n), sign(m) = 0 & n, m = 0 \\ sign(n), sign(m) = -1 & n, m < 0 \end{cases} \quad (1.5)$$

It should be noted that aspect is not defined if slope is zero.

Curvatures (κ)

Curvature calculation is considered difficult due to the fact that different curvatures can be obtained in different directions, depending on the purposes (Mitášová and Hofierka 1993). Profile curvature is in the direction of the gradient and signifies the change of slope angle, which is a governing factor for the change in velocity of mass flowing down along slope curve (Krcho 1973; Young 1978; Mitášová and Hofierka 1993; Olaya 2008).

$$\kappa_{Prof} = -\frac{m^2 \cdot i + 2m \cdot n \cdot i \cdot j + n^2 \cdot k}{(m^2 + n^2)\sqrt{(1 + m^2 + n^2)^3}} \quad (1.6)$$

where $i = \partial^2 z/\partial x^2$; $j = \partial^2 z//\partial x \partial y$; and $k = \partial^2 z/\partial y^2$.

Tangential curvature is measured normal to the plane in the direction perpendicular to gradient and it is always tangent to the contours (Mitášová and Hofierka 1993; Olaya 2008).

$$\kappa_{Tan} = -\frac{n^2 \cdot i - 2m \cdot n \cdot j + m^2 \cdot k}{(m^2 + n^2)\sqrt{1 + m^2 + n^2}} \quad (1.7)$$

Plan curvature is in the direction perpendicular to gradient and measures the change in aspect angle, in which the divergence or convergence of flowing water is dictated. Normally, this

is measured in a horizontal plane (Evans 1972; Krcho 1973; Mitášová and Hofierka 1993; Olaya 2008).

$$\kappa_{Plan} = -\frac{n^2 \cdot i - 2m \cdot n \cdot j + m^2 \cdot k}{\sqrt{(1+m^2+n^2)^3}} \tag{1.8}$$

Mean curvature is the average of profile and tangential curvatures. It shows the mean concavity or convexity, in which accumulations are given by positive values (Young 1805; Olaya 2008).

$$\kappa_{Mean} = \frac{1}{2}\left(\kappa_{Prof} + \kappa_{Tan}\right) \tag{1.9}$$

1.1.4. Surface topographic parameters (STP) tool

The STP tool (Figure 1.3) is designed to compute the aforementioned topographic parameters. The outputs can be displayed in tabular and graphic formats. Its user's interface consists of seven command buttons and one combo box to enable flexibility of options.

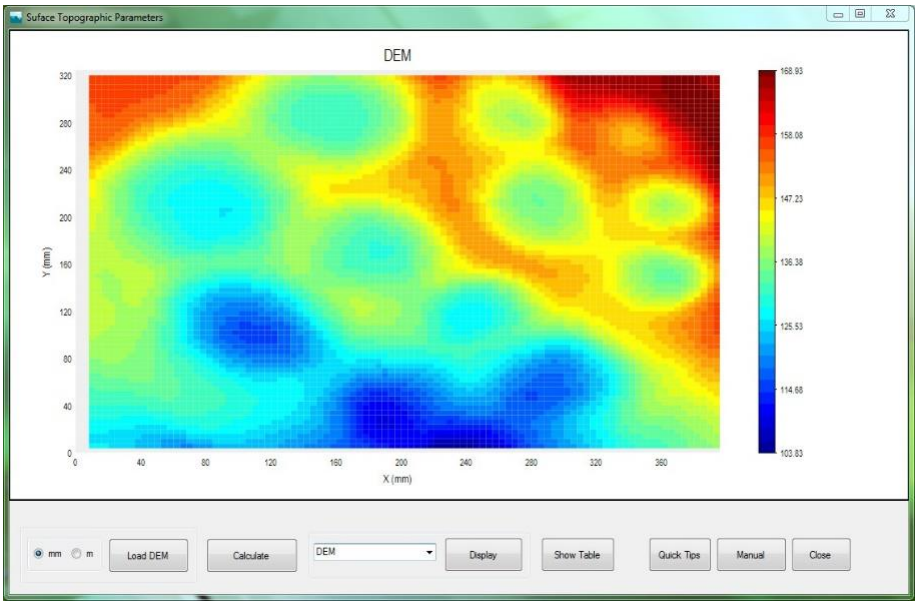

Figure 1.3. Main interface of STP tool

1.1.5. Introduction to Puddle Delineation (PD) program

Chu et al. (2010) detailed the PD program (Figure 1.4), which has been used in this study for DEM-based puddle identification and characterization. The PD implements a new approach for the identification of puddle cells, centers, thresholds, flats, and levels, storage volume, maximum depression storage (MDS), maximum ponding area (MPA), and the relationships of multiple puddles, which ultimately are used in modeling of the puddle-to-puddle dynamic process. The PD search algorithm involves eight neighboring cells (top, bottom, right, and left) in addition to the cell in focus (central cell). If a cell has an elevation lower than its eight neighboring cells is termed as a center. If multiple cells are identified as centers they form a flat. The puddle spilling point is called threshold. The minimum criterion for a puddle is that it should have at least one center and one threshold. When one or more puddles share a threshold they may combine to form a larger puddle which is referred as a higher level puddle. Multiple higher level puddles may eventually merge to form the highest level puddle. Once all such hierarchical relationships are identified, puddle property parameters including puddle storage at all levels, MDS, MPA, and puddle depths are calculated. The PD program also determines flow directions and accumulations, and computes slopes and other microtopographic parameters. The PD program provides essential surface delineation data and microtopographic parameters for the P2P model.

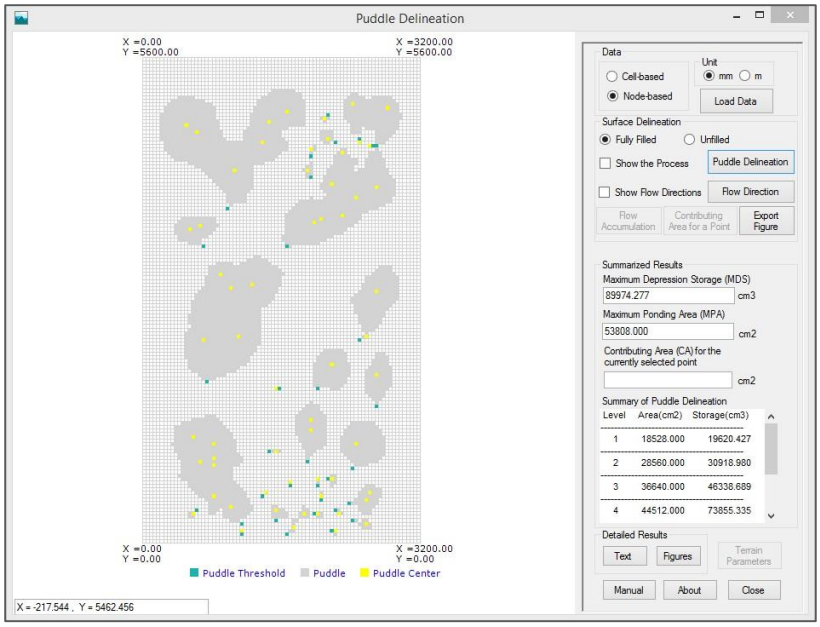

Figure 1.4. Main interface of PD program

1.2. Introduction to P2P Modeling System

The P2P modeling system (Figure 1.5) (Chu et al. 2013a and b) was utilized in this study for characterization of surface microtopography and physically-based modeling of dynamic P2P filling-spilling-merging-splitting overland flow processes, infiltration, and unsaturated flow. The P2P model is a quasi-3D, distributed model that simulates overland flow across a topographic surface as well as infiltration and unsaturated flow in heterogeneous soils under complex rainfall events that may include both wet and dry time periods. It features a hierarchical modeling framework (Chu et al. 2013a). The input data of the model primarily include surface topographic data from the PD program, and the data/parameters associated with spatial and temporal discretization (e.g., row and column of DEM grids, soil layers and cells, time interval, and total simulation period), rainfall, evaporation, soil properties, initial surface ponding, and initial soil moisture condition. The P2P model provides all details on both spatial and temporal variations in surface ponding, P2P filling-spilling-merging dynamics, overland flow, infiltration, unsaturated flow, and hydrologic connectivity. The results can be displayed using the built-in

2D/3D visualization tools or using a table or text format. My part in the P2P model was partial interface programming.

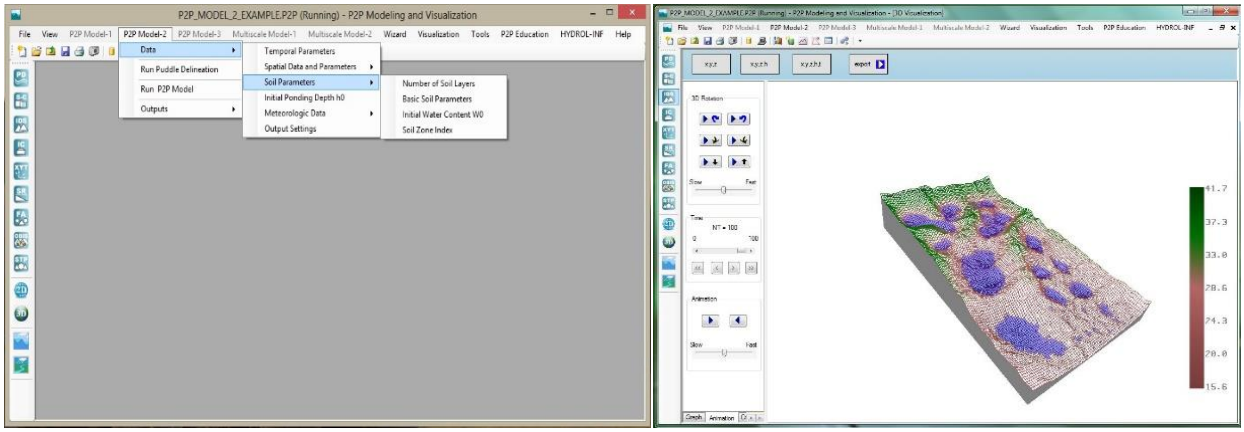

Figure 1.5. Main interface of the Windows-based P2P modeling system and 3D distribution of simulated surface ponding areas

In the P2P system, a modified Green-Ampt model (Chu and Marino 2005; Chu and Marino 2006) was used for simulating infiltration and unsaturated flow. This infiltration module can simulate infiltration through a layered soil profile of an arbitrary moisture distribution under any complex rainfall input (steady, unsteady, and multiple events). For the wet time period, the wetting front movement is tracked and the shift between ponding and non-ponding surface conditions is simulated. Once a particular rainfall event stops, the drainage and redistribution module takes over the task of simulating the soil moisture movement. In the P2P, different forms of Richards equations are used for vertical soil moisture drainage and redistribution.

Based on the PD results, the P2P model automatically divides the entire topographic surface into basins and puddle based units (PBUs). PBU includes a puddle and its contributing area or the cells that are draining to the puddle, while a basin can include one or more PBUs (Chu et al. 2013a). PBUs may discharge to another downstream PBU or to the outlet when water level reaches the threshold thereby forming a cascading drainage network. No contribution is expected from PBU before the threshold is reached. In the P2P model, overland flow is routed

within each PBU for all respective cells (Cell to Cell (C2C) routing) and for all puddles in/between PBUs (P2P routing). Once all PBUs are connected, MDS will be reached and the entire surface will contribute runoff water to the outlet(s).

The hydrologic connectivity of a topographic surface is interrupted by surface depression and as such it is represented by a series of spatially distributed hydrologically connected areas (ACs). Yang and Chu (2013) proposed a concept of P2P hydrologic connectivity to characterize hydrologic connectivity related to the P2P dynamics. The structural hydrologic connectivity (Antoine et al. 2009; Lexartza-Artza and Wainwright 2009) of a topographic surface reflects the static microtopographic properties of the surface and is subject to changes only by geomorphologic processes. Another indicator is functional hydrologic connectivity (Bracken and Croke 2007), which characterizes the dynamic changes and evolution of ACs and their linkage/separation to/from the outlet(s). The properties of ACs and MDS are functions of surface microtopography and puddle characteristics, and their evolution is strongly affected by the dynamic P2P processes (Yang and Chu 2013).

1.3. Objectives

The overall goal of my research is to model surface microtopography and the related hydrologic processes. Specifically, the objectives of this thesis research are: (1) to evaluate the effects of DEM resolution on microtopographic characteristics, hydrologic connectivity, and modeling of hydrologic processes; and (2) to assess the influences of multiple rainfall events on surface and subsurface processes with the use of the P2P modeling system.

The purpose of Chapter 1 was to provide a brief overview of surface microtopography and the associated factors that affect hydrologic modeling; and an introduction to the P2P

modeling system. Moreover, DEM- and image-based approaches that are used for topographic surface characterization were introduced.

The objective of Chapter 2 was to show the effects of DEM resolution on microtopographic characteristics, hydrologic connectivity, and modeling of hydrologic processes. Specifically, this chapter covered the spatial and temporal changes in hydrologic connectivity, surface depression storage, infiltration as DEM resolution changed. The effects of DEM resolution on surface runoff and MDS were also discussed. Analysis of several microtopographic characteristics was included and the chapter as a whole described the interrelationships of surface microtopographic characteristics, hydrologic connectivity, and various hydrologic processes.

The objective of Chapter 3 was to quantify the effects of multiple rainfall events on surface and subsurface processes. The changes in spatio-temporal distributions of infiltration and surface depression storage, initial moisture condition, and wetting front movement that were induced by different rainfall events were discussed. Moreover, this chapter also covered the effects of multiple rainfall events on hydrologic connectivity, depression filling time, and the time to reach maximum depression storage.

1.4. References

Antoine, M., Javaux, M., and Bielders, C. (2009). "What indicators can capture runoff relevant connectivity properties of the micro-topography at the plot scale?" *Advances in Water Resources,* 32(8), 1297–1310.

Blaschke, T. (2010). “Object based image analysis for remote sensing.” *ISPRS Journal of Photogrammetry and Remote Sensing*, 65, 2–16.

Bracken, L. J., and Croke, J. (2007). "The concept of hydrological connectivity and its contribution to understanding runoff-dominated geomorphic systems." *Hydrological Processes,* 21, 1749–1763.

Chu, X., Marino, M. A. (2006). "Simulation of infiltration and surface runoff - A Windows-based hydrologic modeling system HYDROL-INF," p1-8. In: *Examining the Confluence of Environmental and Water Concerns, Proceedings of the 2006 World Environmental and Water Resources Congress*, edited by R. Graham. American Society of Civil Engineers.

Chu, X., and Marino, M. A. (2005)." Determination of ponding condition and infiltration into layered soils under unsteady rainfall." *Journal of Hydrology,* 313(3-4), 195–207.

Chu, X., Yang, J., Chi, Y., and Zhang, J. (2013a)." Dynamic puddle delineation and modeling of puddle-to-puddle filling-spilling-merging-splitting overland flow processes." *Water Resources Research*, 49(6), 3825–3829.

Chu, X., Zhang, J., Yang, J., Habtezion, N., Chi, Y., and Yang, Y. (2013b). *P2P Modeling System, User's Manual*, Version 1.50, North Dakota State University.

Chu, X. (2011). "Characterization of microtopography and its hydrologic significance" (Chapter 1), p1–14. In: *Modeling Hydrologic Effects of Microtopographic Features,* edited by X. Wang. Nova Science Publishers, Inc.

Chu, X., Zhang, J., Chi, Y., and Yang, J. (2010). "An improved method for watershed delineation and computation of surface depression storage", p1113-1122. In: Watershed Management 2010: Innovations in Watershed Management Under Land Use and Climate Change, Proceedings of the 2010 Watershed Management Conference, edited by K. W. Potter and D. K. Frevert. American Society of Civil Engineers.

Darboux, F., Davy, Ph., Gascuel-Odoux, C., Huang, C. (2001). “Evolution of soil surface roughness and flowpath connectivity in overland flow experiments.” *Catena*, 46, 125-139.

Darboux, F., and Huang, C. (2003). “An instantaneous-profile laser scanner to measure soil surface microtopography.” *Soil Science Society of America Journal*, 67, 1, sci. mod. 92.

Drăguţ, L., and Eisank, C. (2012). “Automated object-based classification of topography from SRTM data.” *Geomorphology*, 141-142, 21–33.

Evans, I. S. (1972). "General geomorphometry, derivatives of altitude, and descriptive statistics." In: Chorley, R.J. (Ed.), Spatial Analysis in Geomorphology. Harper & Row, 17–90.

Govers, G., Takken, I., and Helming, K. (2000). “Soil roughness and overland flow.” *Agronomie*, 20, 131–146.

Huang, C., and Bradford, J. M. (1990). “Depressional storage for Markov-Gaussian surfaces.” *Water Resources Research*, 26(9), 2235–2242.

Huang, C., and Bradford, J. M. (1992). “Application of a laser scanner to quantify soil microtopography.” *Soil Science of Society America Journal*, 56, 14–21.

Jain, A. K. (2010). “Data clustering: 50 years beyond K-means.” *Pattern Recognition Letters*, 31, 651–666.

Krcho, J. (1973). "Morphometric analysis of relief on the basis of geometric aspect of field theory." *Acta Geographica Universitatis Comenianae, Geographico-Physica*, 1 (1), 7–233.

Lexartza-Artza, I., and Wainwright, J. (2009). "Hydrological connectivity: linking concepts with practical implications." *Catena*, 79(2), 146–152.

MacMillan, R. A., Martin, T. A., Earle, T. J., and McNabb, D. H. (2003). “Automated analysis and classification of landforms using high-resolution digital elevation data: applications and issues.” *Canadian Journal of Remote Sensing*, 29 (5), 592–606.

Mitášová, H., and Hofierka, J. (1993). “Interpolation by regularized spline with tension, II Application to terrain modelling and surface geometry analysis.” *Mathematical Geology*, 25, 657–669.

Olaya, V. (2008). “Basic land-surface parameters,” Chapter 6. In: *Geomorphometry: Concepts, Software, Applications. Developments in Soil Science Series*, vol. 33, T. Hengl and H. I. Reuter (Eds), Elsevier, p141–169.

Pennock, D. J., Zebarth, B. J., and de Jong, E. (1987). "Landform classification and soil distribution in hummocky terrain." *Geoderma*, 40, 297–315.

Pike, R. J., Evans, I. S., Hengl, T. (2008). "Geomorphometry: a brief guide,” Chapter 1. In: *Geomorphometry: Concepts, Software, Applications. Developments in Soil Science Series*, vol. 33, T. Hengl and H. I. Reuter (Eds), Elsevier, p3–30.

Schiewe, J. (2002). “Segmentation of high-resolution remotely sensed data concepts applications and problems.” Symposium on Geospatial Theory, Processing and Applications, Ottawa.

Shary, P. A., Sharaya, L. S., and Mitusov, A. V. (2002). "Fundamental quantitative methods of land surface analysis." *Geoderma*, 107 (1–2), 1–32.

Wright, Jr. R. S., Lipchak, B., and Haemel, N. (2007). *OpenGL SuperBible: Comprehensive Tutorial and Reference*, 4th Ed., Pearson Education Inc., Boston, MA.

Yang, J., and Chu, X. (2013). "Quantification of the spatio-temporal variations in hydrologic connectivity of small-scale topographic surfaces under various rainfall conditions." *Journal of Hydrology*, 505, 65–77.

Young, M. (1978). "Terrain analysis: program documentation. Report 6 on Grant DA-ERO-591-73-G0040." *Statistical characterization of altitude matrices by computer*, Department of Geography, University of Durham, Durham, UK, 27.

Young, T. (1805). "An essay on the cohesion of fluids." *Philosophical Transactions of the Royal Society of London*, 95, 65–87.

Zalik, K. R. (2008). “An efficient k-means clustering algorithm.” *Pattern Recognition Letters*, 29, 1385–1391.

CHAPTER 2. EFFECTS OF DEM RESOLUTION ON MICROTOPOGRAPHIC CHARACTERISTICS, HYDROLOGIC CONNECTIVITY, AND MODELING OF HYDROLOGIC PROCESSES

2.1. Abstract

The resolution of a digital elevation model (DEM) is one of the crucial factors that need due consideration in watershed hydrologic and environmental modeling. DEM resolution (or grid size) can cause significant variability in the representation of surface topography, which further affects quantification of hydrologic connectivity and simulation of hydrologic processes. The objective of this study is to examine the effects of DEM resolution on (1) surface microtopographic characteristics, (2) hydrologic connectivity, and (3) the spatial and temporal variations of hydrologic processes including infiltration, surface depression storage, evaporation, and surface runoff. A puddle-to-puddle (P2P) modeling system was utilized for surface delineation and modeling of the P2P overland flow dynamics, surface runoff, infiltration, and unsaturated flow for nine DEM resolution scenarios. Comparisons of the simulation results for the nine modeling scenarios demonstrated that coarser DEM resolutions tended to eliminate topographic features, further reduce surface depression storage, infiltration, and evaporation, and strengthen hydrologic connectivity and surface runoff. In contrast, finer DEM resolutions captured more detailed microtopographic variations and facilitated more accurate simulation of hydrologic processes. This study emphasizes the importance of DEM resolution in characterization of surface microtopography and its critical role in improvement of hydrologic modeling.

2.2. Introduction

Accurate representation of land surface is crucial to watershed hydrologic and environmental modeling. Distributed hydrologic models have been successfully utilized in conjunction with land surface models for hydrologic studies as the spatial and temporal distributions of hydrologic processes are dictated by surface topography. Digital elevation models (DEMs), which are available at different resolutions and scales, have been used as a data source to derive topographic and hydrologic attributes. However, no universal DEM exists, which can be used for different purposes without any bias. Thus, the biggest challenge to the modeling is how to identify the right DEM with the right resolution and scale.

Studies have been conducted to evaluate the influences of DEM resolution (or grid size) on hydrologic analysis and modeling. Yang and Chu (2013a) investigated the effects of DEM resolution on surface depression properties and hydrologic connectivity, and analyzed the relationships and distributions of depression property parameters for various microtopographic surfaces with different DEM resolutions. They demonstrated the remarkable influences of DEM resolution on microtopographic characteristics and hydrologic connectivity. Wu et al. (2008) evaluated the effects of DEM resolution on topographic derivatives including slope, upslope contributing area, flow length, and watershed area. Zhang and Montgomery (1994) found that slope, drainage area per unit contour length, topographic index, surface saturation, and catchment's response to a storm event varied with DEM grid sizes for the same watersheds. Thompson et al. (2001) compared terrain attributes and quantitative soil-landscape models originated from grid based DEMs and found that terrain attributes varied spatially as a result of variations in DEM resolutions. Wolock and Price (1994) used TOPMODEL to show the effects of both DEM map scale and data resolution on the statistics of topographic index distribution and

prediction. Sørensen and Seibert (2007) also emphasized dissimilar topographic wetness indices resulted from different DEM resolutions. Li and Wong (2010) analyzed different DEM resolutions and sources and found that accurate stream networks could be extracted from higher resolution DEMs although it might not always be the case. In addition, they underlined that higher resolution data had a lesser impact on flood simulation. Charrier and Li (2012) concluded that DEM resolution had a great impact on flood plain delineation and also pointed out that coarser DEMs could be more appropriate for flood plain modeling and analysis as fine resolution DEMs were more sensitive to small topographic changes. Wang and Yin (1998) used the ArcGIS depression filling algorithm and obtained similar results for USGS DEMs with scales of 1:24,000 and 1:250,000. Vaze et al. (2010) conducted a statistical analysis and presented a good comparison between LiDAR DEMs and field surveyed elevation data although the LiDAR DEMs were better than the elevation data derived from contour maps. They found that both accuracy and resolution of a DEM play an important role in the resulting hydrologic spatial indices. Zhang et al. (2014) studied the impacts of DEM resolution on hydrology and non-point source (NPS) contaminants in their SWAT modeling. Dixon and Earls (2009) evaluated the sensitivity of stream flow to DEM resolution using ArcSWAT and showed dissimilar modeling results between the original DEM and the resampled one. Lin et al. (2010) concluded that DEM resolution might affect uncertainty analysis.

In addition, traditional DEM-based delineation often involves depression filling (fill sink) and surface reconditioning, which impose a permanent change in the original DEM and also potentially affect the subsequent modeling (Callow et al. 2007). Such models fail to directly account for the significance of surface depressions. In summary, the influences of DEM resolution on hydrologic modeling have been extensively studied for different conditions and

various purposes. However, some important issues still remain unaddressed. For example, how does DEM resolution affect specific hydrotopographic processes that are well connected and have intrinsic interactions? The focus of this study is on quantifying the changes in the interrelated microtopographic and hydrologic processes induced by different DEM resolutions. The specific objective of this study is to examine the effects of DEM resolution on (1) surface microtopographic characteristics, (2) hydrologic connectivity, and (3) the spatial and temporal variations of hydrologic processes including infiltration, surface depression storage, evaporation, and surface runoff. To achieve the objective, surface delineation and puddle-to-puddle (P2P) overland flow modeling are performed for nine DEM resolution scenarios and the simulation results are analyzed and compared.

2.3. Materials and Methods

2.3.1. Modeling scenarios

The area of the topographic surface selected for this modeling study was 179,200 cm^2 (560 × 320 cm) (Figure 2.1). The soil profile was discretized into 2.5-mm cells. The total simulation period was 100 min, which consisted of 100 time steps (i.e., time interval Δt = 1 min). The original surface was scanned in the field by using an instantaneous-profile laser scanner (Chu et al. 2010). Bogart (2014) described the detailed procedures regarding the field experiment setup. This study utilized the experimental data and focused on modeling. The horizontal and vertical resolutions of the laser scanner were 0.98 and 0.5 mm, respectively. Based on the original DEM, nine different resolution DEMs (grid size DX = 2, 4, 5, 8, 10, 16, 20, 40, and 80 cm) were created by employing the Kriging method. These specific grid sizes were selected because they produced square grids that covered the entire field plot. Figures 2.1a-2.1d show four selected DEMs. In the analyses of most results, these four DEM grid sizes will be used.

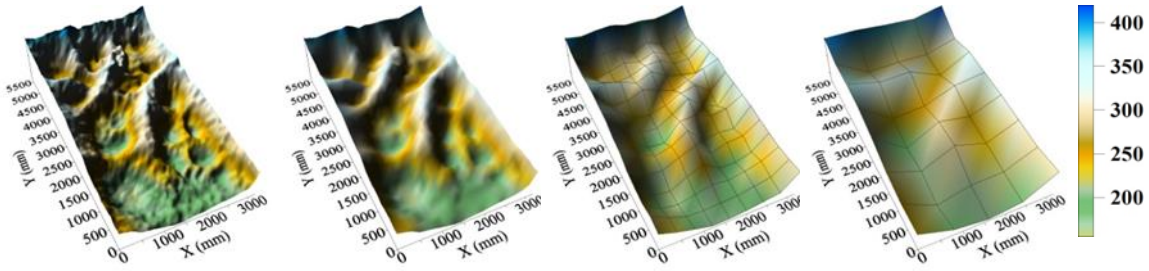

(a) DX = 4 (b) DX = 16 cm (c) DX = 40 cm (d) DX = 80 cm

Figure 2.1. DEMs for four selected DEM grid sizes (DX = 4, 16, 40, and 80 cm)

Nine modeling scenarios (M1 - M9) corresponding to the nine DEM resolutions were created to evaluate the impacts of DEM resolution on microtopographic characteristics, hydrologic connectivity, and hydrologic processes simulated by the P2P model. For all modeling scenarios, identical rainfall, soil type, and initial soil moisture content (θ_0) were used. A 30-min unsteady rainfall event was applied to a sandy clay loam soil surface. The intensities of the unsteady rainfall were 5.0 cm/hr at t = 0 - 10 min, 8.0 cm/hr at t = 11 - 20 min, 5.0 cm/hr at t = 21 - 25 min, and 3 cm/hr at t = 26 - 30 min. There was no rain during the remaining time steps (i.e., t = 31 - 100 min). It was assumed that the soil and rainfall were uniformly distributed across the soil surface. Thus, only one soil zone and one rainfall zone were considered in the P2P modeling. Table 2.1 shows the soil hydraulic parameters for the selected soil (sandy clay loam). A uniform distribution of initial soil moisture (θ_0 = 0.2 cm^3/cm^3) was assumed.

Table 2.1. Major soil hydraulic parameters [a]

Parameters	Values
Saturated hydraulic conductivity K_s (cm/h)	1.31
Suction head h_s (cm)	21.85
Saturated water content θ_s (cm^3/cm^3)	0.39
Residual water content θ_r (cm^3/cm^3)	0.10
Soil water retention parameter n	1.48
Soil water retention parameter α (1/cm)	0.059

[a] Carsel and Parrish, 1988.

2.3.2. Hydrologic connectivity analysis

The P2P filling-spilling-merging-splitting dynamics characterize overland flow generation (Chu et al. 2013a and b). The structural hydrologic connectivity (Antoine et al. 2009; Lexartza-Artza and Wainwright 2009) of a topographic surface is derived from its DEM. It reflects the static microtopographic properties of the surface and is subject to changes only by some geomorphologic processes. Another indicator is functional hydrologic connectivity (Bracken and Croke 2007), which characterizes the dynamic changes and evolution of hydrologically connected areas (ACs) and their linkage/separation to/from the outlet(s) as a result of puddle filling, spilling, merging, and splitting during and after a rainfall event. Such a hierarchical connecting and separating process was referred to as P2P hydrologic connectivity (Yang and Chu 2013b). Thus, structural hydrologic connectivity quantifies the microtopography-determined static hydrologic connectivity, while functional hydrologic connectivity describes the dynamic connectivity due to the threshold-driven P2P process (Yang and Chu 2013b).

In the P2P model, P2P hydrologic connectivity is used to characterize the static and dynamic states of hydrologic connectivity. It is portrayed by a network of contiguous polygons that are formed by contributing cells, puddle cells, or the combination of the two. From the temporal point of view, P2P hydrologic connectivity can be described by two stages. Structural hydrologic connectivity reflects the static connectivity pattern of the surface that is resulted from the spatial configuration of cells, which will not change until a surface ponding condition is established. Functional hydrologic connectivity reveals the dynamic connectivity pattern that is altered as a function of the dynamic P2P filling-spilling-merging-separating process. This study focused on the analyses of structural hydrologic connectivity (t = 0) and functional hydrologic connectivity at three critical time steps (t = 10, 30, and 100 min).

2.4. Results and Discussions

2.4.1. Effects of DEM resolution on surface microtopographic characteristics

The PD program in the P2P modeling system provided details on the surface microtopographic characteristics. Table 2.2 summarizes the related microtopographic attributes for the nine surfaces of different DEM resolutions, including the number and size of DEM cells, total surface area, number of puddles and puddle levels, number of the first and highest level puddles, number of basins, mean slope, MDS, MPA, mean contributing area (MCA), mean of the maximum puddle water depths, and mean of average puddle water depths. The relationships between DEM grid size and these topographic parameters are shown in Figure 2.2.

Table 2.2. Surface microtopographic property parameters

DEM grid size DX (cm)	2	4	5	8	10	16	20	40	80
Number of rows	280	140	112	70	56	35	28	14	7
Number of columns	160	80	64	40	32	20	16	8	4
Total number of cells	44,800	11,200	7,168	2,800	1,792	700	448	112	28
Surface area (cm^2)	179,200	179,200	179,200	179,200	179,200	179,200	179,200	179,200	179,200
Number of puddle levels	9	7	5	4	3	3	3	1	1
Number of puddles	102	69	57	38	32	22	19	4	2
Number of the highest-level puddles	36	31	21	14	14	12	9	4	2
Number of the first-level puddles	69	50	39	26	23	17	14	4	2
Number of basins	4	4	3	2	1	1	1	1	1
Mean slope (%)	17.68	17.24	16.79	15.90	15.24	13.26	12.02	7.45	4.01
MDS (cm^3)	90,863	88,687	87,791	84,435	81,502	64,035	58,578	21,121	2,220
MPA (cm^2)	54,148	53,312	52,575	50,688	49,100	43,776	41,600	20,800	12,800
MCA (cm^2)	16,095	15,863	15,778	15,856	15,935	16,131	17,072	14,471	23,543
Mean of maximum puddle depths (cm)	1.21	1.39	1.93	2.58	2.41	2.01	2.01	1.63	0.17
Mean of average puddle depths (cm)	0.49	0.57	0.80	1.09	1.06	0.92	0.90	0.67	0.09

Notes: MDS = maximum depression storage; MPA = maximum ponding area; and MCA = mean contributing area.

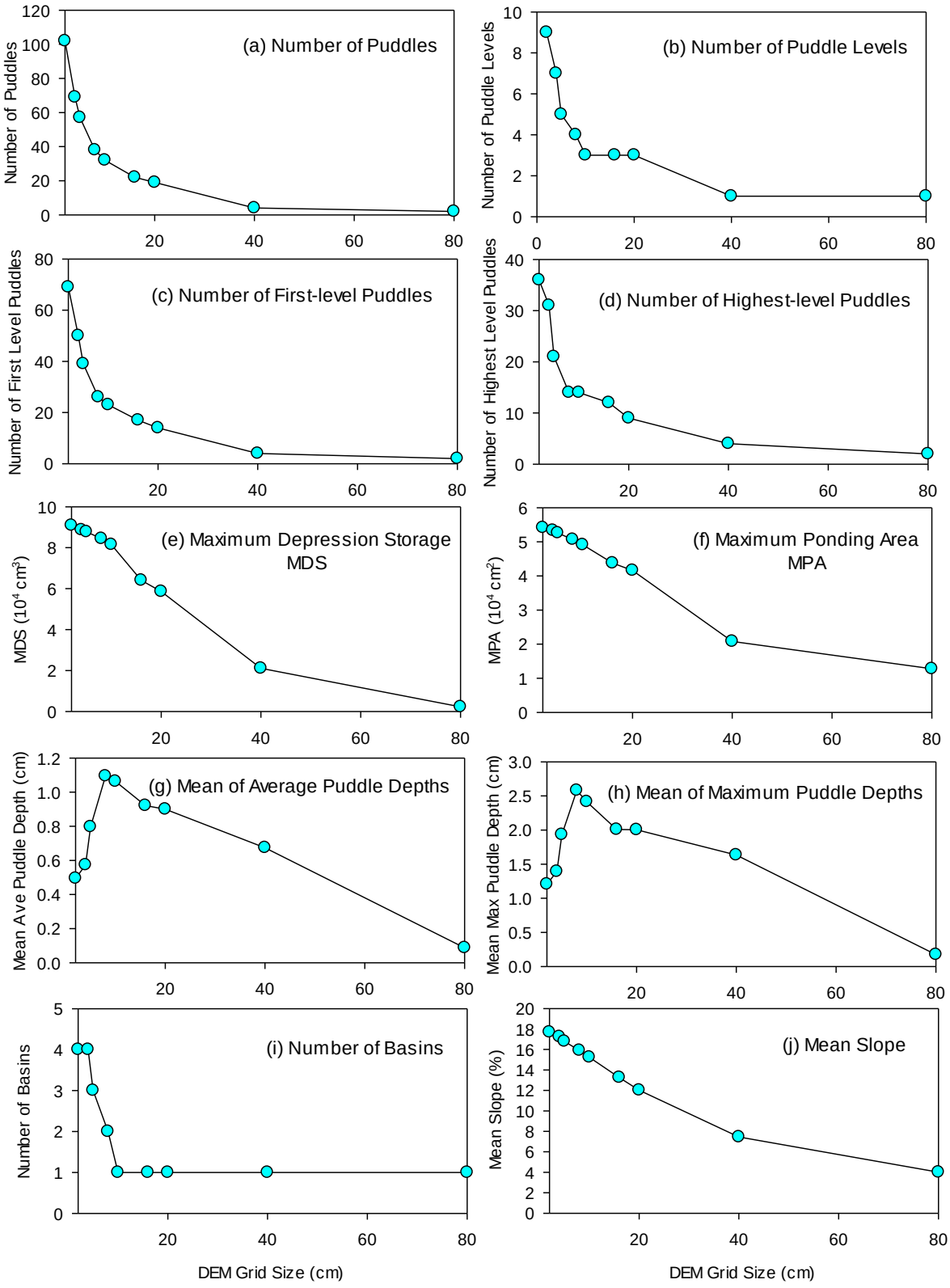

Figure 2.2. Relationships between DEM grid size and surface topographic parameters

Lowering the DEM resolution significantly affected the microtopographic properties of the surface. The 2-cm resolution surface was represented by 44,800 cells, but this number dramatically decreased to 28 when the DEM grid size increased to 80 cm (Table 2.2). Resultantly, the microtopographic features of paramount hydrologic significance (e.g., small depressions and peaks) were eliminated (Figure 2.1d). Due to the "smoothing and aggregation" effect and the decrease in the number of DEM grids that were used to represent the surface topography, the total number of puddles decreased from 102 for the 2-cm DEM resolution to 2 for the 80-cm DEM resolution (Table 2.2, Figure 2.2a). Similar reduction in the puddle levels and the numbers of the first- and highest-level puddles can be observed as the DEM grid size increased from 2 to 80 cm (Table 2.2, Figures 2.2b-2.2d). Particularly, significant decreases in these values occurred when the grid size was smaller than 20 cm (Figure 2.2a-2.2d).

Both MDS and MPA of the surface also declined with an increase in DEM grid size due to the loss of topographic information and the decrease in the number of puddles (Figures 2.2e and 2.2f). The MDS and MPA of the 2-cm resolution surface were 90,863 cm^3 and 54,148 cm^2, respectively, while they decreased to 2,220 cm^3 and 12,800 cm^2 for the 80-cm resolution surface (Table 2.2). These two microtopographic parameters followed a similar decreasing trend. The mean of average puddle depths and the mean of maximum puddle depths were also affected by the change in DEM resolution. Unlike MDS and MPA, however, these two parameters exhibited a dissimilar changing pattern. Both increased within a range of smaller DEM grid sizes (higher resolution) and then decreased with an increase in DEM grid size (lower resolutions). The mean of average puddle depths was 0.49 cm at DX = 2 cm, reached the peak of 1.09 cm at DX = 8 cm, and then decreased to 0.09 cm at DX = 80 cm (Table 2.2, Figure 2.2g). Similarly, the mean of maximum puddle depths increased from 1.21 to 2.58 cm as the DEM grid size increased from 2

to 8 cm and afterwards it declined to 0.17 cm when the DEM grid size increased to 80 cm (Table 2.2, Figure 2.2h). This changing pattern can be attributed to the mechanism of aggregation of DEM grids and the averaging effect when creating coarser DEMs. For high resolution DEMs (DX ≤ 8 cm), a coarser resolution surface may have fewer deeper depressions than a finer resolution surface that may consist of more and shallower depressions.

The number of basins and the mean slope of a topographic surface are important to the related hydrologic processes. The smoothing effect imposed by the decrease in DEM resolutions tended to change the original surface to a more uniform surface. This affected the number of basins and the mean slope of the surface. The number of basins of the field plot reduced from 4 to 1 and the mean slope decreased from 17.68% to 4.01 % when the DEM grid size increased from 2 to 80 cm (Table 2.2, Figures 2.2i and 2.2j). This effect on the surface delineation eventually affected hydrologic connectivity and all hydrologic processes simulated in the model. Also it should be noted that some DEM grid sizes may produce the same number of basins (e.g., DX = 2 - 4 cm and DX = 10 - 80 cm in Figure 2.2i) and the minimum number of basins for a surface is one.

2.4.2. Effects of DEM resolution on hydrologic connectivity

Figure 2.3 shows the evolution of hydrologic connectivity, the dynamic change of connected areas, and the spatial distributions of ponded water at three different time steps (t = 10, 30, and 100 min) for the four selected DEM grid sizes (4, 16, 40, and 80 cm). The selected time steps represent three important stages of hydrologic connectivity. Figures 2.3a-2.3c respectively show the states of hydrologic connectivity at t = 10 min (soon after the ponding condition was achieved), t = 30 min (end of the rainfall period), and t = 100 min (end of the entire simulation period). It can be observed that the number of connected areas decreased with an increase in the

DEM grid size DX. The 4-cm DEM captured more microtopographic details of the surface and hence the functional hydrologic connectivity was characterized by more polygons (i.e., connected areas). It took a longer time to achieve the complete hydrologic connectivity. For DX = 80 cm, however, the isolated areas were quickly connected after the ponding condition was achieved at t_p = 7.51 min. This can be attributed to the change in the nature and configuration of topographic elements as a result of the change in DEM resolution. The 80-cm resolution surface consisted of continuous planes (large DEM grids) that resulted in higher structural hydrologic connectivity. The depressions on this coarser resolution surface were not real topographic features. Instead, they were pits created by the DEM grid planes of different elevations (Figure 2.3a4).

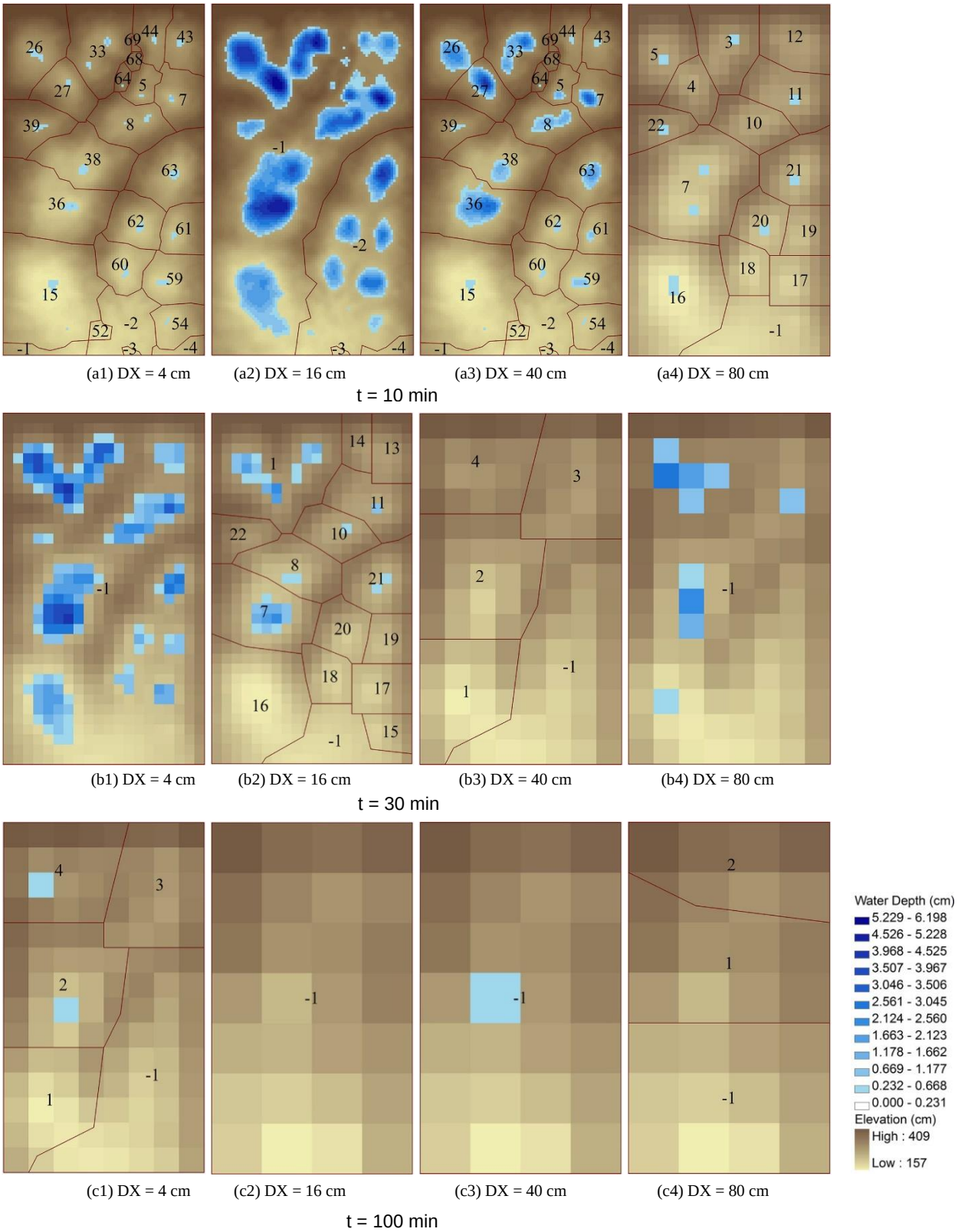

Figure 2.3. Functional hydrologic connectivity at t = 10, 30, and 100 min for four selected DEM grid sizes (DX = 4, 16, 40, and 80 cm)

Figures 2.4-2.7 show the distributions and statistics (including total number N, mean μ, standard deviation σ, minimum, and maximum) of connected areas at t = 0, 10, 30, and 100 min for the DEM grid sizes of 4, 16, 40, and 80 cm. The distributions of connected areas at t = 0 min indicate the pre-rainfall hydrologic connectivity or structural hydrologic connectivity, while all others show the functional hydrologic connectivity. After the ponding condition was achieved, the number of connected areas reduced and ultimately the number of bars in the chart equaled the number of outlets for a particular DEM resolution. To better describe the distribution of connected areas for a selected time step and DEM resolution, an exponential function was fitted and basic statistical parameters were calculated and shown in Figures 2.4-2.7.

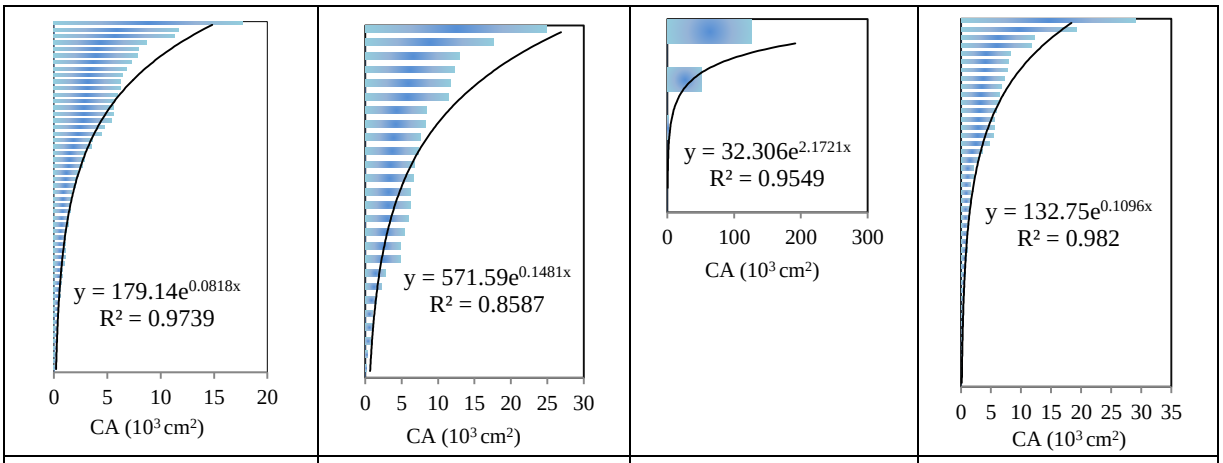

(a) t = 0 min	(b) t = 10 min	(c) t = 30 min	(d) t = 100 min
N = 54 μ = 3,319 σ = 3,593 Min = 96 Max = 17,632	N = 26 μ = 6,892 σ = 5,773 Min = 224 Max = 24,960	N = 4 μ = 44,800 σ = 59,071 Min = 288 Max = 125,888	N = 45 μ = 3,982 σ = 5,552 Min = 96 Max = 29,104

Figure 2.4. Distribution and statistics of connected areas CA (total number N, mean μ, standard deviation σ, minimum, and maximum) at t = 0, 10, 30, and 100 min for DEM grid size of 4 cm

The 4-cm resolution surface consisted of 54 connected areas before the rainfall event (t = 0 min) (Figure 2.4a). This number reduced to 26 at t = 10 min (Figure 2.4b). In other words, the number of connected areas decreased as some connected areas were getting bigger. By the fully-

filled time (i.e., when the MDS was reached), the entire surface had 4 distinct areas, two of which were significantly larger, as indicated by the change in standard deviation σ (Figure 2.4c). At the end of the simulation time period (t = 100 min), the surface was represented by 45 connected areas (Figure 2.4d), indicating that there were still certain connected areas left due to the presence of ponded water (Figure 2.3c1).

The 16-cm resolution surface had a smaller number of connected areas (18) at the beginning of the modeling time period (Figure 2.5a), and it reduced to 15 at t = 10 min (Figure 2.5b). By the time of full hydrologic connectivity, the whole surface was represented by only one area (Figure 2.5c). At t = 100 min, the surface was depicted by 16 connected areas (Figure 2.5d), which was smaller than the number of connected areas (18) at t = 0 min, indicating an existence but lower ponded water on the surface (Figure 2.3c2).

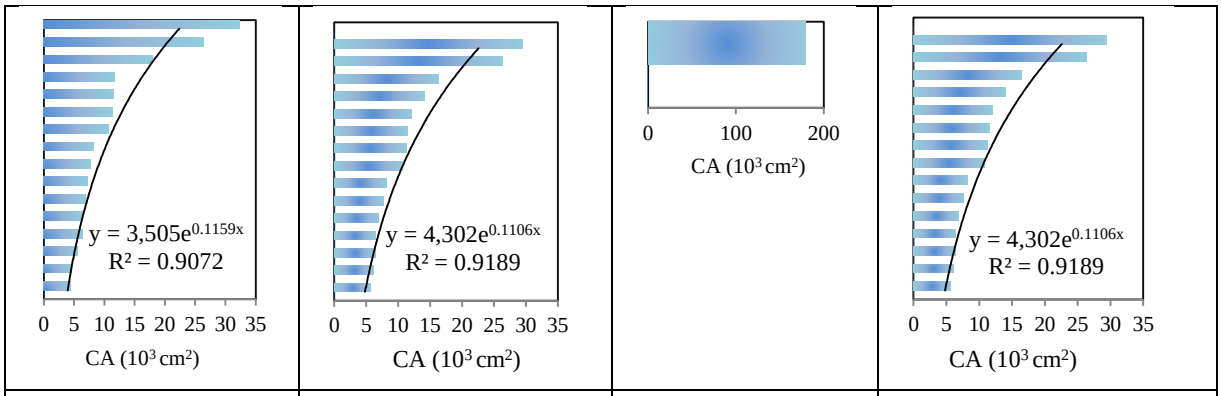

(a) t = 0 min	(b) t = 10 min	(c) t = 30 min	(d) t = 100 min
N = 18 μ = 9,956 σ = 5,456 Min = 4,352 Max = 26,368	N = 15 μ = 11,947 σ = 7,236 Min = 5,632 Max = 29,440	N = 1 μ = 179,200 σ Min = 179,200 Max = 179,200	N = 16 μ = 11,200 σ = 7,928 Min = 4,352 Max = 32,256

Figure 2.5. Distribution and statistics of connected areas CA (total number N, mean μ, standard deviation σ, minimum, and maximum) at t = 0, 10, 30, and 100 min for DEM grid size of 16 cm

The distributions of connected areas for DX = 40 and 80 cm were similar (Figures 2.6 and 2.7). There were 5 connected areas at t = 0 and 10 min (Figures 2.6a and 2.6b), and this

number reduced to 1 at the time of maximum connectivity (Figure 2.6c) for DX = 40 cm. The 80-cm resolution surface included 3 connected areas at t = 0 min (Figure 2.7a), and 1 connected area at t = 10 and 30 min (Figures 2.7b and 2.7c) when full connectivity was prevailed. By the end of the modeling time period (t = 100 min), the connected areas on both surfaces (DX = 40 and 80 cm) increased to the original numbers at t = 0 min (i.e., 5 and 3 for DX = 40 and 80 cm, respectively) (Figures 2.6d and 2.7d). This can be attributed to the fact that the 40-cm resolution surface had a very small amount of ponded water stored in the first-level puddles (Figures 2.3c3) and that no ponded water existed on the 80-cm resolution surface at t = 100 min (Figure 2.3c4).

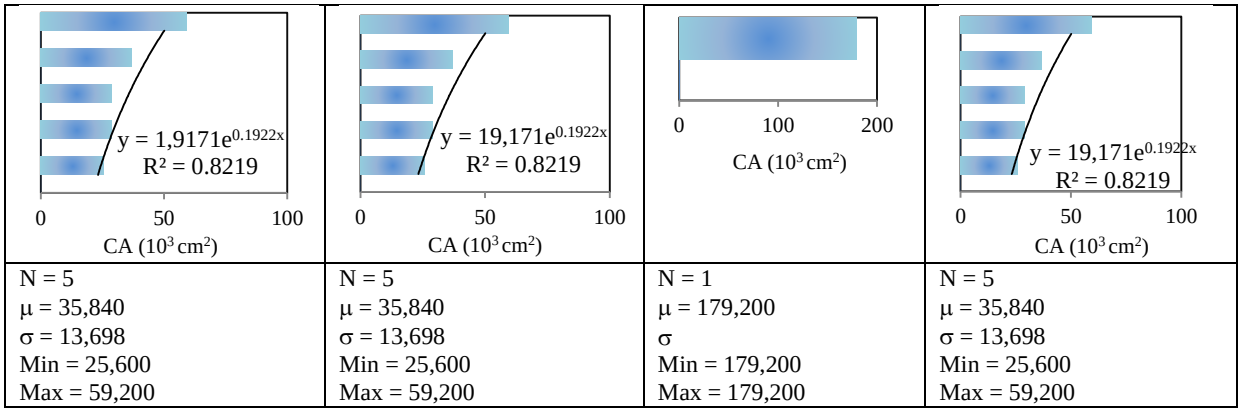

(a) t = 0 min	(b) t = 10 min	(c) t = 30 min	(d) t = 100 min
N = 5 μ = 35,840 σ = 13,698 Min = 25,600 Max = 59,200	N = 5 μ = 35,840 σ = 13,698 Min = 25,600 Max = 59,200	N = 1 μ = 179,200 σ Min = 179,200 Max = 179,200	N = 5 μ = 35,840 σ = 13,698 Min = 25,600 Max = 59,200

Figure 2.6. Distribution and statistics of connected areas CA (total number N, mean μ, standard deviation σ, minimum, and maximum) at t = 0, 10, 30, and 100 min for DEM grid size of 40 cm

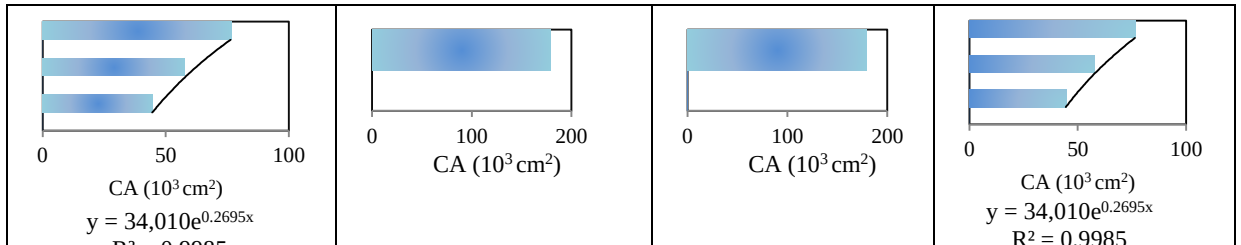

a) t = 0 min	(b) t = 10 min	(c) t = 30 min	(d) t = 100 min
N = 3 μ = 59,733 σ = 16,106 Min = 44,800 Max = 76,800	N = 1 μ = 179,200 σ Min = 179,200 Max = 179,200	N = 1 μ = 179,200 σ Min = 179,200 Max = 179,200	N = 3 μ = 59,733 σ = 16,106 Min = 44,800 Max = 76,800

Figure 2.7. Distribution and statistics of connected areas CA (total number N, mean μ, standard deviation σ, minimum, and maximum) at t = 0, 10, 30, and 100 min for DEM grid size of 80 cm

For all the selected DEM resolutions, MDS was reached before the end of the rainfall event (t = 30 min). Thus, the functional hydrologic connectivity at t = 30 min depicted a fully matured connectivity pattern. For DX = 16, 40, and 80 cm, the whole topographic surface was represented by one basin when functional hydrologic connectivity was at its peak, while the surface of 4-cm DEM resolution included two major basins and two small basins (Figures 2.3b1 – 2.3b4). This affected the average of connected areas. Figure 2.8a shows the temporal changes in average connected areas for the four DEM resolutions (DX = 4, 16, 40, and 80 cm). Time lags can be observed for the curves in Figure 2.8a, in addition to the differences in their peaks. Ultimately, all curves leveled off at their peaks although they occurred at different time steps. The leveled off portion of each curve shows the period at which the MDS was maintained. The curve of the 80-cm DEM surface was the earliest one to level off while the 4-cm DEM curve leveled off much later. At the full maturity of functional hydrologic connectivity, the average connected area was 44,800 cm^2 for the 4-cm DEM grid size. This indicates that the average connected area depended on the number of basins, and more basins resulted in a lower peak. For the 4-cm resolution surface, the total area was divided into four basins. After the end of rainfall event (t = 30 min), the curves plunged dramatically (Figures 2.8a). This was due to the sharp transition from fully matured functional hydrologic connectivity to a very earlier stage of functional hydrologic connectivity. At this stage, the 4-cm resolution curve had a slightly gradual change, compared with all other resolution curves. During the dry time period (t = 30 - 100 min), the ponded water decreased; some higher-level puddles were separated into their lower-level embedded puddles; and more puddles were depleted due to evaporation and infiltration. Resultantly, more areas were disconnected and the number of connected areas increased at the end of the modeling period (t = 100 min) (Figures 2.3c1 – 2.3c4, Figures 2.8b). Also due to the

puddle splitting process, more lower-level puddles were formed. For the coarser DEM resolutions, the surface depression storage became empty before the end of the modeling period and hence the functional hydrologic connectivity was equivalent to the structural hydrologic connectivity of the surface (Figure 2.3c4, Figure 2.8c). Note that the structural hydrologic connectivity increased in accordance with an increase in DEM grid size. Overall, this study demonstrated that hydrologic connectivity was significantly affected by DEM resolution and it varied with the topographic details of a surface and its MDS.

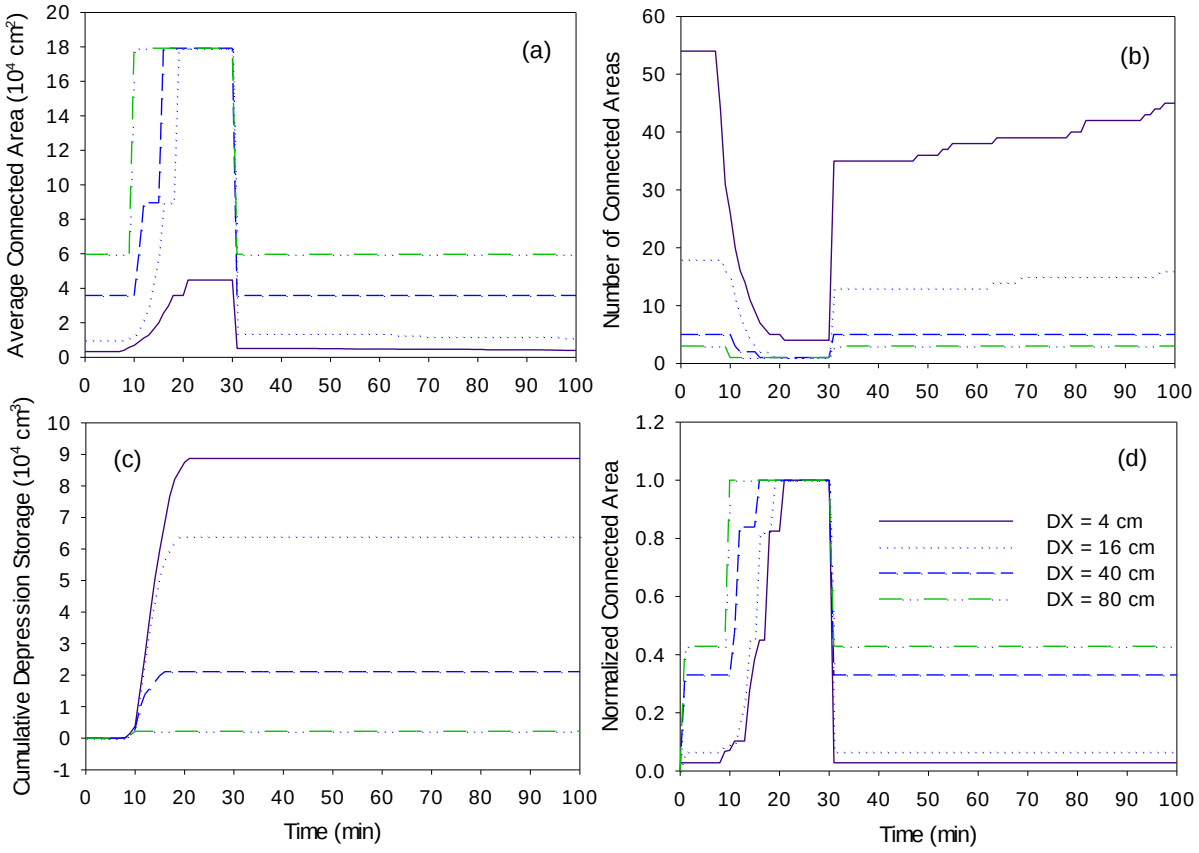

Figure 2.8. Temporal distributions of (a) average connected area, (b) number of connected areas, (c) cumulative depression storage, and (d) normalized connected area (ratio of the area connected to the outlet to the total surface area) for four selected DEM grid sizes (DX = 4, 16, 40, and 80 cm)

For a larger DEM grid size (e.g., DX = 80 cm), the quick response of depressions to the P2P process on the corresponding surface facilitated the connection or separation of

hydrologically connected areas (Figure 2.8b). Due to the characteristics and sizes of the depressions, the linkage of connected areas to the final outlet became instant during the time of rainfall. As soon as rainfall stopped, the connected areas were detached immediately. In contrast, a surface with a finer DEM resolution (e.g., DX = 4 cm) exhibited a more gradual connection and disconnection process (Figure 2.8b). Also, at the time of puddle spilling and merging (connection) the number of connected areas was declining very steeply. After the rainfall stopped, the disconnection process also became gradual as indicated by the gentle slopes (Figure 2.8b). This can be attributed to the fact that surface depression filling was faster than depression depleting which resulted from slower infiltration and evaporation. The depth of the "valley" curves increased proportionally to the number of connected areas and DEM grid size. Hence, the 4-cm resolution surface had an NCA curve with the deepest "valley" while the 80-cm resolution surface had the shallowest one (Figure 2.8b). Figure 2.8c shows the temporal variations of cumulative surface depression storage as a result of the expansion of connected areas. The finest DEM resolution (DX = 4 cm) had the highest ordinate signifying the highest surface depression storage. There were remarkable differences among the ordinates for the four grid sizes (4, 16, 40, and 80 cm) and all curves leveled off after their MDS values were reached although this happened at different times (Figure 2.8c). The 80-cm resolution surface reached its MDS first and it had the lowest ordinate. Also, the cumulative storage curves showed steeper slopes at the initial stage than the later stage when the surface depression storage was close to the MDS due to the narrow bottom and wider top shape of most depressions. As was evident from Figures 2.8b and 2.8c, changes in DEM grid size affected the number, rearrangement, and configuration of puddles, which resulted in noticeable differences in the number of connected areas and the cumulative surface storage.

Figure 2.8d shows the temporal changes of normalized connected area (NLCA) for the four selected DEM resolutions. NLCA is the ratio of the areas connected to the outlet to the total surface area. At the beginning, the four curves showed different NLCA values. The 80-cm resolution surface had the highest ordinate. For all curves, there was no change in NLCA until the ponding condition was reached at t = 7.51 min, which was depicted by the horizontal portion. The NLCA curves exhibited sudden stepwise increases that were caused by the puddle spilling process. Such a changing pattern continued until their MDS values were reached. The puddle filling process dominated before t = 7, 8, 10, and 9 min for the 4-, 16-, 40-, and 80-cm DEM grid sizes, respectively (Figure 2.8d). After these times, puddle spilling was triggered and the puddles began to contribute runoff to the outlet. Additionally, merging of some puddles and spilling of the associated higher-level puddles induced even greater stepwise increases in the curves. For the 4-cm resolution surface, although the spilling time started earlier, the response of the outlet was slower because of the existence of a greater number of depressions which served as "barriers." The surface reached its MDS at t = 22 min (Table 2.3). However, the 80-cm resolution surface reached its MDS at t = 10 min (Table 2.3) and it took only 2.5 min for the entire surface to become connected to the outlet after the ponding time. The span of the maintained MDS in the curve affected the water budget of the related surface. Once the rainfall stopped, almost all curves plummeted to the state prior to the ponding time (Figure 2.8d), which was the sign of separation of the connected areas.

From this study, it was found that both structural and functional hydrologic connectivity were dependent on DEM grid size. The change in DEM grid size altered the spatial configuration and the size of connected areas even before the rainfall event (i.e., structural hydrologic connectivity). The smoothing and aggregation effect induced by increasing DEM grid size also

resulted in more geometrically connected shapes rather than topographic features such as ridges and depressions. It was found that the pits created from large DEM grid planes had a higher potential to connect to the downstream outlet in addition to a faster filling time. This can be attributed to the regularity of their shapes and reduction in their roughness. An increase in DEM grid size tended to mask smaller-scale microtopographic features that were captured by a higher resolution DEM. Particularly, removal of such important topographic features and reduction in surface roughness further enhanced the continuity of the drainage network and directly affected hydrologic connectivity.

2.4.3. Effects of DEM resolution on simulated hydrologic processes

Due to the changes in DEM grid size, all simulated hydrologic processes, including infiltration, surface depression storage, evaporation, and surface runoff became significantly different. Table 2.3 summarizes the modeling results for the nine scenarios (M1 to M9). Figure 2.9a shows the relationships of DEM grid size and cumulative rainfall, infiltration, surface depression storage, and outlet discharge, while Figure 2.9b displays ponding time and fully-filled time for the nine different DEM grid sizes (2, 4, 5, 8, 10, 16, 20, 40, and 80 cm). Note that all cumulative values on Figure 2.9a correspond to the final simulation results at the last time step (t = 100 min).

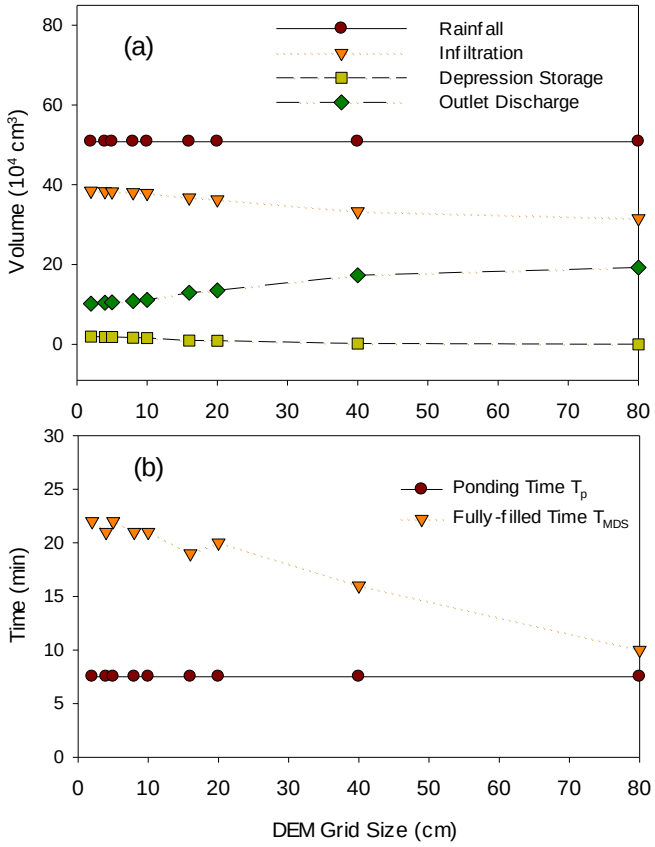

Figure 2.9. Relationships of DEM grid size and (a) cumulative volumes of rainfall, infiltration, surface depression storage, and outlet discharge; (b) ponding time Tp and fully-filled time TMDS

Table 2.3. Modeling results for scenarios M1 – M9 (sandy clay loam soil and unsteady rainfall [a])

Scenario	M1	M2	M3	M4	M5	M6	M7	M8	M9
DX (cm)	2	4	5	8	10	16	20	40	80
P (cm^3)	507,733	507,734	507,733	507,733	507,733	507,733	507,733	507,733	507,733
I (cm^3)	384,423	383,081	382,469	380,682	378,641	367,490	362,588	332,614	315,343
S (cm^3)	19,266	18,439	18,157	16,592	15,704	9,427	8,890	1,550	0
E (cm^3)	2,069	2,030	2,012	1,960	1,902	1,574	1,429	559	62
Q (cm^3)	101,975	104,184	105,095	108,500	111,487	129,242	134,826	173,012	192,329
T_p (min)	7.51	7.51	7.51	7.51	7.51	7.51	7.51	7.51	7.51
MDS (cm^3)	90,863	88,687	87,791	84,435	81,502	64,035	58,578	21,121	2,220
T_{MDS} (min)	22	21	22	21	21	19	20	16	10

Notes: *DX* = DEM grid size; *P* = cumulative rainfall; *I* = cumulative infiltration; *S* = ponded water in surface depressions at last time step; *E* = cumulative evaporation; *Q* = cumulative outlet discharge; T_p = ponding time; *MDS* = maximum depression storage; and T_{MDS} = fully-filled time (i.e., all depressions are fully filled and the system reaches the *MDS* at this time).

[a] 30-min unsteady rainfall (10-min 5 cm/hr, 10-min 8 cm/hr, 5-min 5 cm/hr, and 5-min 3 cm/hr).

As shown in Table 2.3 and Figure 2.9a, with an increase in DEM grid size, the simulated cumulative infiltration decreased approximately linearly by 18.0%, from 384,423 cm^3 for DX = 2 cm to 315,343 cm^3 for DX = 80 cm (Table 2.3, Figure 2.9a). The reduction in MDS with an increase in DEM grid size can be one of the reasons for the decrease in cumulative infiltration. Depressions were serving as a reserve supply for cumulative infiltration after rainfall had ceased and as a barrier to the flowing water so that it was able to infiltrate at a pace of the hydraulic properties of the soil. However, with an increase in DEM grid size the surface lost these characteristics and the rainfall excess quickly left the system without much contribution to the infiltration demand.

By the end of the simulation period (t = 100 min), surface depression storage decreased from 19,266 to 0 cm^3 when the DEM grid size increased from 2 to 80 cm (Table 2.3, Figure 2.9a). This can be attributed to the combined effect of the decrease in MDS and the spatial changes in infiltration and evaporation. Note that MDS was 90,863 cm^3 for DX = 2 cm and 2,220 cm^3 for DX = 80 cm (Table 2.2). Similar to the analysis of the changes in MDS, the increase in DEM grid size induced the loss of topographic details, which in turn resulted in a decrease in surface depression storage.

The cumulative outlet discharge behaved opposite to the cumulative infiltration (Figure 2.9a). Accordingly, whatever did not infiltrate into soil contributed to surface runoff. For DX = 2 cm, the cumulative outlet discharge was 101,975 cm^3 and then surged to 192,329 cm^3 when the DEM grid size increased to 80 cm (Table 2.3, Figure 2.9a), which amounted to an increase of 88.6 %. This large change in the magnitude of discharge can be attributed to the effect of the changes in surface microtopography and the smoothing effect, which was manifested herein by a declining MDS and the response to the declining cumulative infiltration. For a higher resolution

DEM, surface microtopography was highly detailed and consisted of numerous micro-depressions, which increased the volume of water that could be stored on the surface, and further increased the surface detention volume and time. The ramifications of these were stressed by the enhanced infiltration and attenuated peak discharge.

Evaporation is one of the mass balance terms. However, it was much smaller than other hydrologic processes (Table 2.3). At t = 100 min, the cumulative evaporation was only 2,030 cm^3 for the 4-cm resolution surface and 62 cm^3 for the 80-cm resolution surface (Table 2.3). For this reason, evaporation is not shown in Figure 2.9 and also it will not be discussed in detail in the following sections.

As shown in Table 2.3 and Figure 2.9b, the ponding time was 7.51 min for all DEM grid sizes since it depended on the soil hydraulic properties only. This was valid as the same homogeneous soil, identical initial soil moisture distribution, and identical zero initial ponded water (dry surface) were assumed for all DEM resolution scenarios. In terms of depression filling, it took 22 min to fully fill all depressions for the 2-cm resolution surface. This fully-filled time decreased to 10 min when the DEM grid size increased to 80 cm (Table 2.3 and Figure 2.9b). This result was associated with the decrease in MDS due to the smoothing and aggregation effect that was induced by the reduction in DEM resolution.

Figures 2.10a – 2.10d show the temporal changes in incremental precipitation, infiltration, outlet discharge, and surface depression storage for DEM grid sizes of 4, 16, 40, and 80 cm. Before the ponding time (t = 7.51 min), all rainwater infiltrated into soil; and there were no surface depression storage and surface runoff. During the post-ponding period, infiltration started decreasing; surface depression storage started increasing; and eventually surface runoff commenced. This changing pattern can be observed for all the DEM resolution scenarios (Figure

2.10). For the two finer resolution surfaces (DX = 4 and 16 cm), certain time lags between the surface depression storage and outlet discharge curves existed (Figures 2.10a and 2.10b). A larger number of depressions delayed the initiation of surface runoff. Both curves showed a rising limb, a peak, and a recession limb that were consistent with the rainfall changing pattern (Figures 2.10a and 2.10b). For the two coarser resolution surfaces (DX = 40 and 80 cm), the depression storage and outlet discharge curves started increasing immediately after the ponding condition was achieved (Figures 2.10c and 2.10d). Due to fewer depressions on these two surfaces, a considerable portion of the surfaces could directly contribute runoff to the outlet even before reaching their MDS. Besides, as the surface depression storage capacity was smaller, the discharge curves exhibited remarkably higher peaks than the depression storage curves (Figures 2.10c and 2.10d).

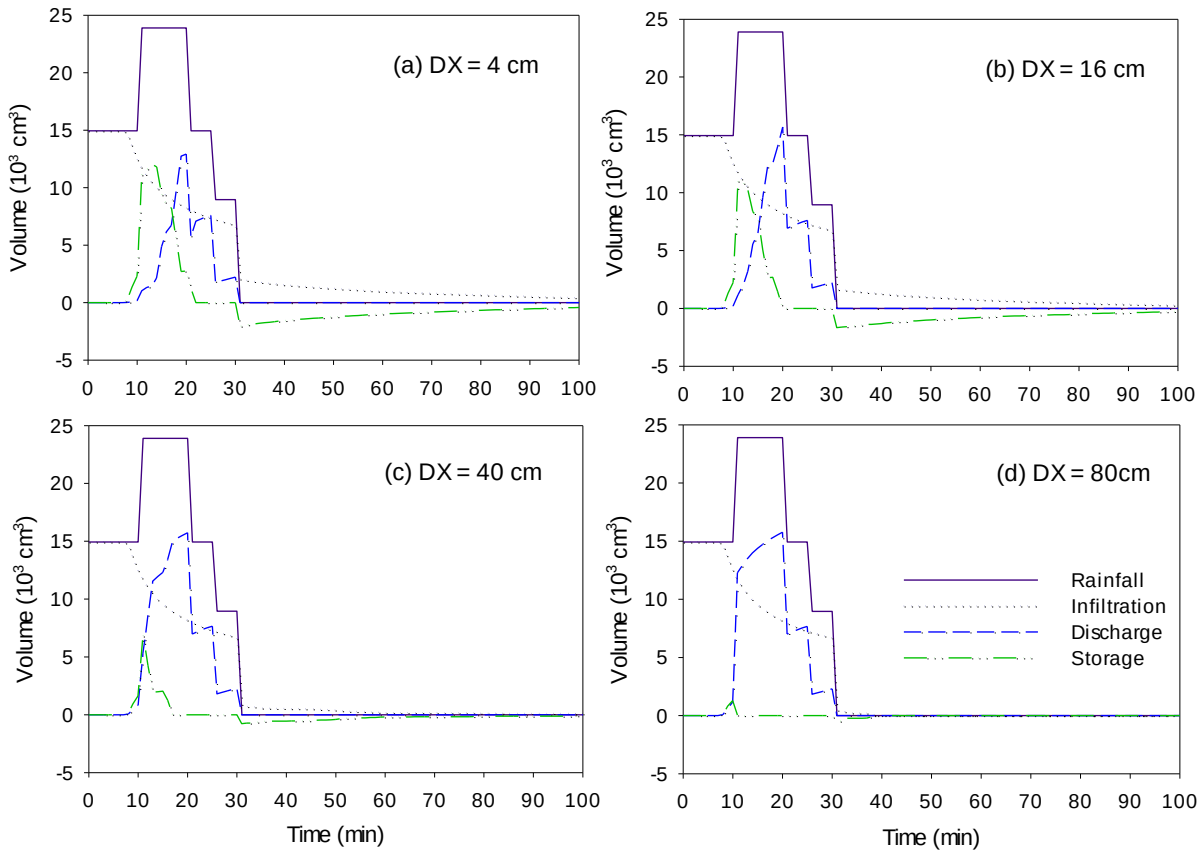

Figure 2.10. Incremental volumes of rainfall, infiltration, outlet discharge, and surface depression storage for four selected DEM grid sizes (DX = 4, 16, 40, and 80 cm)

After rainfall ceased at t = 30 min, depression storage water started depleting (negative values, Figure 2.10) due to infiltration and evaporation. The 4-cm resolution surface had the largest surface depression storage and hence the highest infiltration. Infiltration decreased as surface depression storage became lower during the dry time period. The 80-cm resolution surface had the lowest surface depression storage and hence the lowest infiltration (Figure 2.10).

Figures 2.11a-2.11d show the comparisons of the rates of rainfall, infiltration, depression storage, and outlet discharge for the four selected DEM grid sizes. Under the same rainfall (Figure 2.11a), the infiltration rate was essentially similar during the rainfall period (t = 0 - 30 min) for the four DEM grid sizes (4, 16, 40 and 80 cm) (Figure 2.11b) since the same soil was used. The only possible difference was due to the variations in surface ponding. However, the

hydraulic effect of ponded water depths was minimal and caused a very small difference in infiltration rate within the duration of the rainfall. During the dry time period (t = 30 - 100 min), surface runoff from the connected areas also stopped and the infiltration from all contributing cells became zero. Infiltration only occurred in the water-ponded puddle areas, and as a result, infiltration varied depending on the MDS. The surface with the finest DEM resolution had the largest MDS and gave rise to the greatest infiltration rate while for the surface of the coarsest DEM resolution, infiltration ceased soon after rainfall had stopped. Such differences in infiltration for the four resolution surfaces can be observed in Figure 2.11b. For a given DEM grid size, the soil moisture content, soil water movement, and the depth of wetting front varied with surface microtopography. The existence of depressions sustained the soil saturation for a longer period, which resulted in greater infiltration, deeper wetting front, and higher soil moisture content.

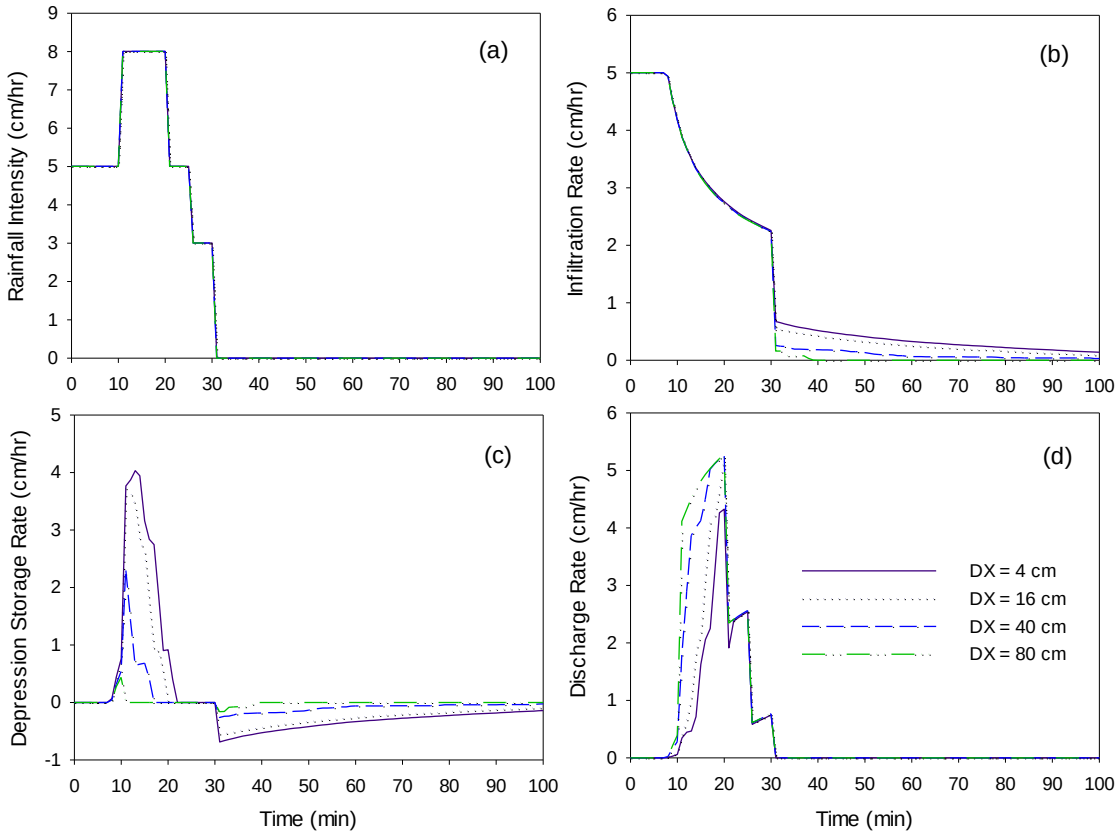

Figure 2.11. Comparisons of the rates of rainfall, infiltration, depression storage, and outlet discharge for four selected DEM grid sizes (DX = 4, 16, 40, and 80 cm)

Significant differences in both magnitude and temporal distribution of surface depression storage can be observed in Figure 2.11c. A surface with a higher DEM resolution had a greater and delayed peak. In the dry period (Figure 2.11c), the decreasing rate of surface depression storage was proportional to the MDS. That is, the water in depressions of a higher resolution surface that had a greater MDS was removed faster, which can be attributed to the larger water-covered area of the surface, resulting in more infiltration and evaporation losses (Figures 2.11c). For all DEM resolution scenarios, the outlet discharge rate increased steadily due to high rainfall intensities, then decreased with reduced rainfall intensities, and eventually reached zero in the dry time period (Figure 2.11d). The 80-cm resolution surface had the highest peak of outlet

discharge and the steepest increasing slope, while the 4-cm resolution surface had the lowest peak and the slowest increase in outlet discharge (Figure 2.11d).

More importantly, the change in DEM grid size significantly affected the spatial distributions of hydrologic variables, such as surface ponding and infiltration. Figure 2.12 shows the spatial distributions of surface ponded water depths at t = 10, 30, and 100 minutes. This was another consequence of the smoothing and aggregation effect induced by the change in DEM resolution. Coarser DEM resolutions averaged surface topographic details. The spatial distribution of ponded water shrank as the DEM grid size increased (Figure 2.12). For the 4-cm resolution surface, sparsely distributed ponded water can be observed for t = 10 min (Figure 2.12a1). At t = 30 min, the ponded water reached its full maturity (MDS and MPA) (Figure 2.12b1). The connected mounds represented the ponded water in higher-lever merged puddles while the isolated ones showed the ponded water in independent puddles. Figure 2.12c1 shows the spatial distribution of ponded water depths at the end of the modeling period. Clearly, many smaller and shallower puddles became empty by t = 100 min, while the remaining puddles still had certain amount of water although their water covered areas had shrunk. The 16-cm resolution surface displayed a similar changing pattern in the ponded water distributions for the three time steps, with the absence of some small puddles (Figures 2.12a2-2.12c2). When the DEM grid size increased to 40 and 80 cm, the distributions of ponded water were very different. The ponded water was extremely low and also localized at limited spots. The 40-cm resolution surface only showed a few mounds of ponded water at t = 30 min (Figures 2.12b3). For the 80-cm resolution surface, the depths of ponded water at t = 10 and 30 min were too small to see on Figures 2.12 a4 and 2.12b4. Note that surface depressions were fully filled at t = 30 min (i.e., its MDS was achieved). The surface was completely drained at t = 100 min (Figure 2.12c4).

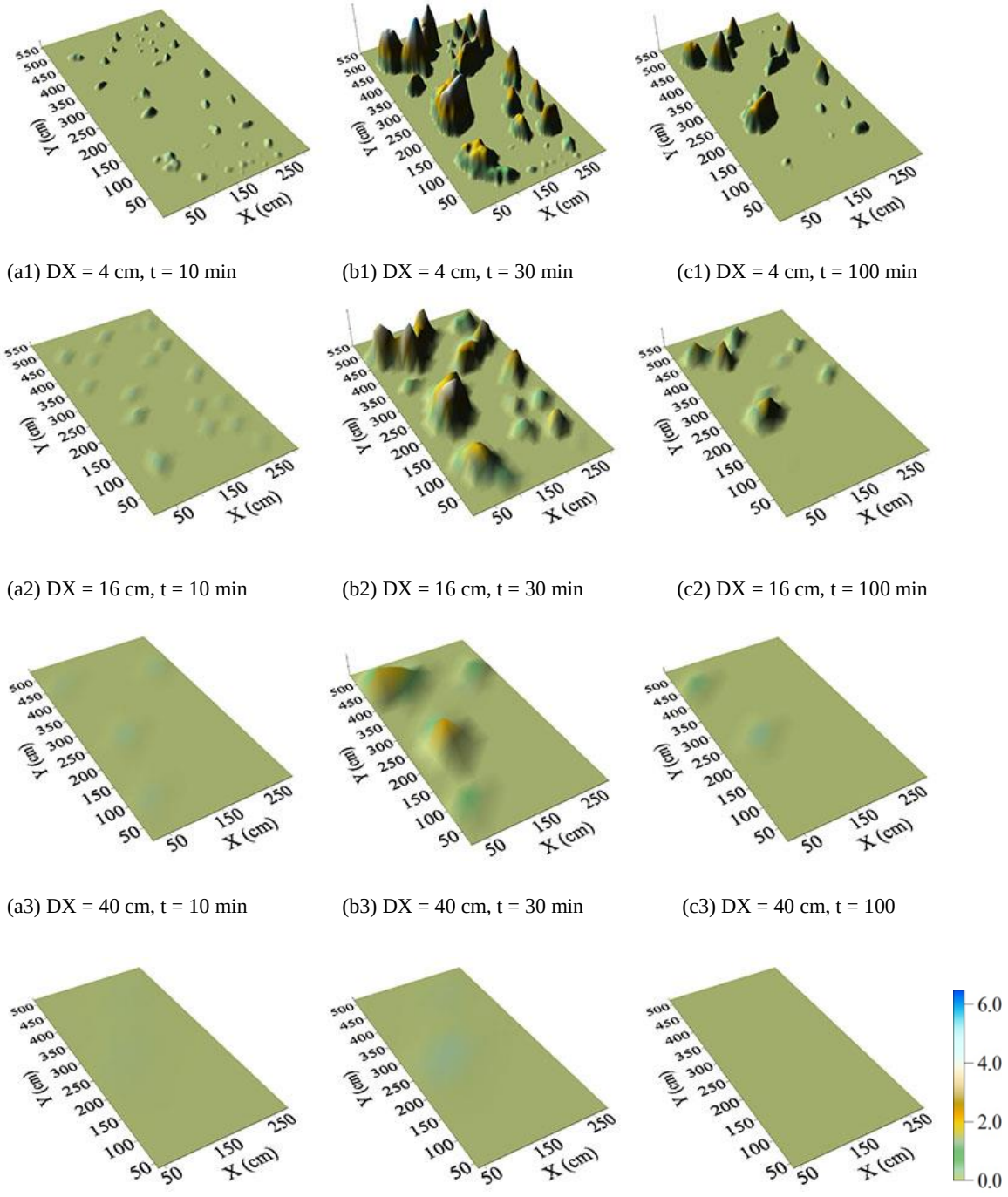

(a1) DX = 4 cm, t = 10 min (b1) DX = 4 cm, t = 30 min (c1) DX = 4 cm, t = 100 min

(a2) DX = 16 cm, t = 10 min (b2) DX = 16 cm, t = 30 min (c2) DX = 16 cm, t = 100 min

(a3) DX = 40 cm, t = 10 min (b3) DX = 40 cm, t = 30 min (c3) DX = 40 cm, t = 100

(a4) DX = 80 cm, t = 10 min (b4) DX = 80 cm, t = 30 min (c4) DX = 80 cm, t = 100 min

Figure 2.12. Spatial distributions of ponded water depths (cm) at t = 10, 30, and 100 min for four selected DEM grid sizes (DX = 4, 16, 40, and 80 cm)

Figure 2.13 shows the comparison of spatial distributions of the simulated cumulative infiltration at the end of the modeling time period (t = 100 min) for the four DEM grid sizes (DX = 4, 16, 40, and 80 cm). Clearly, the change in DEM grid size resulted in significant differences in the spatial distributions of cumulative infiltration. The 4-cm DEM characterized detailed microtopographic variations with a greater number of depressions (Figure 2.1a). The distribution of the simulated cumulative infiltration for this high-resolution surface featured numerous peaks (Figure 2.13a) that were consistent with the distribution of puddles. The distribution of cumulative infiltration for the 16-cm resolution surface (Figure 2.13b) was roughly similar to that of the 4-cm resolution surface. However, some details were missing and the peaks were lower. After further increase in the DEM grid size, more essential details that indicated the infiltration variability disappeared. As shown in Figure 2.13c, the 40-cm resolution DEM only captured a few infiltration peaks located at the major large puddles. Due to fewer shallower depressions on such a low-resolution surface, there was less ponded water for infiltration. When the DEM grid size increased to 80 cm, the spatial distribution of the simulated cumulative infiltration was almost planar (Figure 2.13d). Overall, the spatial distribution of cumulative infiltration matched the variability in surface microtopography. Cumulative infiltration declined with increasing DEM grid size and its peaks were located in puddle areas.

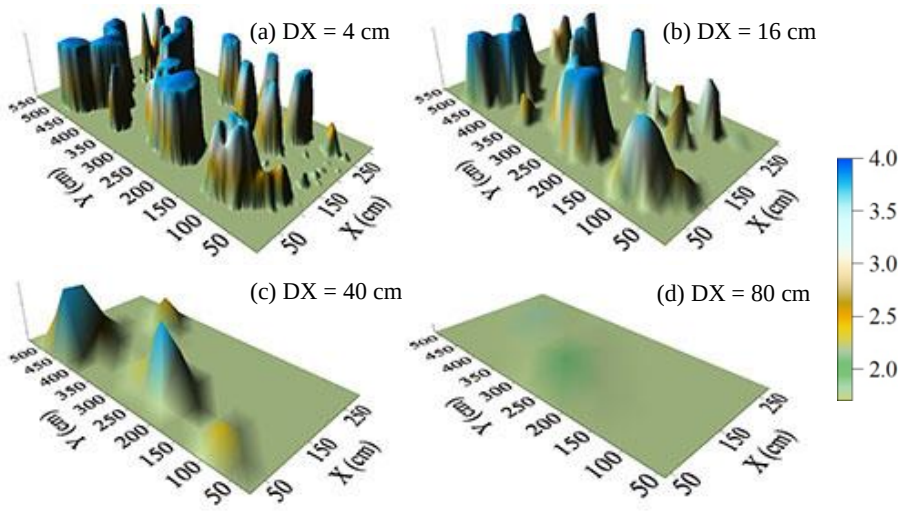

Figure 2.13. Spatial distributions of cumulative infiltration (cm) at t = 100 min for four selected DEM grid sizes (DX = 4, 16, 40, and 80 cm)

2.5. Summary and Conclusions

This study highlighted the significance of DEM resolution and evaluated its impacts on characterization of surface microtopography, quantification of hydrologic connectivity, and simulation of hydrologic processes. Nine DEM resolution scenarios were considered; puddle delineation and P2P overland flow modeling were conducted for the corresponding topographic surfaces; and the results were analyzed and compared. The findings from this study would potentially help select proper DEM data and improve the capabilities of a DEM-based hydrologic model that is often scale dependent.

The change in DEM resolution had a significant effect on how surface microtopography was depicted. Full representation of the natural heterogeneity of a topographic surface was not possible as a result of the smoothing and aggregation effect induced by increasing DEM grid size, which tended to eliminate important topographic features. The mean and maximum puddle depths were affected by DEM resolution and interpolation/aggregation of DEMs. A coarser resolution DEM tended to remove surface depressions and lower the MDS. The number of

basins and the mean slope declined as a result of smoothing for coarser DEM resolutions. Ultimately, a topographic surface became a single basin with a smoother surface.

DEM grid size affected both structural and functional hydrologic connectivity. Reduction in DEM resolution tended to "enhance" hydrologic connectivity and resulted in early maturity of functional hydrologic connectivity. In contrast, a higher resolution DEM captured more detailed topographic features and the relevant surface was subject to smaller-scale dynamic processes before it reached a fully-connected status. Coarser resolution DEMs exhibited the propensity to mask the effect of important land surface features, ultimately creating a surface that consisted of a number of large planar DEM grids and resulting in virtually highly connected areas. During a rainfall event, the topographic elements of the surface became more responsive to connectivity. That is, they became connected soon after surface ponding occurred and disconnected instantly once rainfall ceased. Overestimation of functional hydrologic connectivity and underestimation of MDS induced by coarser DEM resolutions resulted in more surface runoff. For a higher resolution surface, however, the connection/separation to/from the downstream outlet was delayed and featured with a stepwise variation pattern. This can be attributed to the greater number of puddles, more connected areas, and larger MDS. This finding highlighted the dependence of functional hydrologic connectivity on the microtopographic characteristics (e.g., number of puddles, their sizes, and their hierarchical relationships).

The change in DEM resolution also altered hydrologic processes simulated in the model. As the DEM grid size became larger, the topographic heterogeneity and roughness of a natural surface were reduced and the filling time of depressions was shortened, which in turn caused higher outlet discharge even at earlier stages of the rainfall period. Surface ponded water depth decreased with an increase in DEM grid size. The spatial distribution of ponded water depths

strongly depended on DEM grid size. The influence of DEM resolution on infiltration mainly occurred after rainfall stopped. The spatial distribution of cumulative infiltration was strongly affected by DEM resolution, which was primarily associated with puddles and their distributions. The greater MDS of a higher resolution surface sustained infiltration for a prolonged period of time, maintained higher soil moisture content, and yielded a deeper wetting front.

2.6. References

Antoine, M., Javaux, M, Bielders, C. (2009). "What indicators can capture runoff relevant connectivity properties of the micro-topography at the plot scale?" *Advances in Water Resources,* 32(8), 1297–1310.

Bogart, D. (2014). "Hydrologic experiments and analysis - the effect of microtopography on runoff generation." M.S. Thesis, North Dakota State University, Fargo, North Dakota.

Bracken, L. J., and Croke, J. (2007). "The concept of hydrological connectivity and its contribution to understanding runoff-dominated geomorphic systems." *Hydrological Processes,* 21, 1749–1763.

Callow, J. N., Van Niel, K. P., Boggs, G. S. (2007). "How does modifying a DEM to reflect known hydrology affect subsequent terrain analysis?" *Journal of Hydrology,* 332, 30–39.

Carsel, R. F., Parrish, R. S. (1988). "Developing joint probability distributions of soil water retention characteristics." *Water Resources Research,* 24(5), 755–769.

Charrier, R., and Li, Y. (2012). "Assessing resolution and source effects of digital elevation models on automated floodplain delineation: A case study from the Camp Creek Watershed, Missouri." *Applied Geography,* 34, 38–46.

Chu, X., Yang, J., Chi, Y., and Zhang, J. (2013a). “Dynamic puddle delineation and modeling of puddle-to-puddle filling-spilling-merging-splitting overland flow processes.” *Water Resources Research,* 49(6), 3825–3829.

Chu, X., Zhang, J., Yang, J., Habtezion, N., Chi, Y., and Yang, Y. (2013b). *P2P Modeling System, User's Manual*, Version 1.50, North Dakota State University.

Chu, X., Zhang, J., Chi, Y., and Yang, J. (2010). “An improved method for watershed delineation and computation of surface depression storage.” In *Watershed Management 2010: Innovations in Watershed Management Under Land Use and Climate Change, Proc. of the 2010 Watershed Management Conf.,* 1113-1122. K. W. Potter and D. K. Frevert, eds. Reston, Va.: ASCE.

Dixon, B., and Earls, J. (2009). “Resample or not? Effects of resolution of DEMs in watershed modeling.” *Hydrological Processes* 23, 1714–1724.

Lexartza-Artza, I., and Wainwright, J. (2009). “Hydrological connectivity: linking concepts with practical implications.” *Catena,* 79(2), 146–152.

Li, J., and Wong, D. W. S. (2010). “Effects of DEM sources on hydrologic applications.” *Computers, Environment and Urban Systems* 34, 251–261.

Lin, K., Zhang, Q., and Chen, X. (2010). “An evaluation of impacts of DEM resolution and parameter correlation on TOPMODEL modeling uncertainty.” *Journal of Hydrology,* 394, 370–383.

Sørensen, R., and Seibert, J. (2007). “Effects of DEM resolution on the calculation of topographical indices: TWI and its components.” *Journal of Hydrology,* 347, 79–89.

Thompson, J. A., Bell, J. C., and Butler, C. A. (2001). “Digital elevation model resolution: effects on terrain attribute calculation and quantitative soil-landscape modeling.” *Geoderma,* 100, 67–89.

Vaze, J., Teng, J., and Spencer, G. (2010). “Impact of DEM accuracy and resolution on topographic indices.” *Environmental Modelling & Software*, 25, 1086–1098.

Wang, X., and Yin, Z. -Y. (1998). “A comparison of drainage networks derived from digital elevation models at two scales.” *Journal of Hydrology*, 210, 221–241.

Wolock, D. M., and Price, C. V. (1994). “Effects of digital elevation model map scale and data resolution on a topography-based watershed model.” *Water Resources Research*, 30(11), 3041–3052.

Wu, S., Li, J., and Huang, G. H. (2008). “A study on DEM-derived primary topographic attributes for hydrologic applications: Sensitivity to elevation data resolution.” *Applied Geography*, 28, 210–223.

Yang, J., and Chu, X. (2013a). "Effects of DEM resolution on surface depression properties and hydrologic connectivity." *Journal of Hydrologic Engineering,* 18(9), 1157–1169.

Yang, J., and Chu, X. (2013b). "Quantification of the spatio-temporal variations in hydrologic connectivity of small-scale topographic surfaces under various rainfall conditions." *Journal of Hydrology,* 505, 65-77.

Zhang, P., Liu, R., Bao, Y., Wang, J., Yu, W., and Shen, Z. (2014). "Uncertainty of SWAT model at different DEM resolutions in a large mountainous watershed." *Water Research*, 53, 132–144.

Zhang W., and Montgomery, D. R. (1994). "Digital elevation model grid size, landscape representation, and hydrologic simulations." *Water Recourses Research*, 30(4), 1019–1028.

CHAPTER 3. EFFECTS OF MULTIPLE RAINFALL EVENTS ON SURFACE AND SUBSURFACE PROCESSES

3.1. Abstract

Temporal rainfall distribution is one of the most important factors that alter the hydrology and water balance of a given system. Rate of infiltration, soil water dynamics, surface water ponding and accumulation, and generation and propagation of surface runoff are some of the hydrologic phenomena which are affected by the pattern of rainfall. To highlight the effects of temporal rainfall distribution on the aforementioned hydrologic variables, a field-plot scale modeling was performed using a quisi-3D distributed hydrologic model – puddle-to-puddle (P2P) modeling system. Three different synthetic multiple rainfall distributions were applied on the field plot surface. The first and second rainfall distributions (RF1 and RF2) had two events each, while the third rainfall distribution (RF3) had three events. After comparing the simulation results for the three rainfall distributions, it was found that the spatio-temporal distributions of infiltration, ponded surface water, hydrologic connectivity, ponding time, time to reach maximum depression storage (MDS) and soil water dynamics were different for all the rainfall events considered. On the first rainfall event, moisture movement was faster in puddle cells, while in the subsequent events it became slower. On the later events, cumulative infiltration and ponding time decreased significantly while the time to reach MDS was generally shorter. In addition, due to the enhancement of hydrologic connectivity the entire topographic surface became connected to the final outlet(s) relatively faster, which ultimately resulted in higher surface runoff generation. Overall, the temporal rainfall distribution significantly affected the hydrologic processes.

3.2. Introduction

The soundness and accuracy of any hydrologic model depend on the number of factors considered and the level of approximation assumed when conceptualizing a real system. One of the important aspects that can affect surface and subsurface hydrology of a system is temporal distribution of rainfall. Infiltration, surface depression storage, evaporation, surface runoff, hydrologic connectivity, surface ponding time, time to reach maximum depression storage, depth of wetting front, and subsurface moisture drainage and redistribution are some of the hydrologic variables that are affected by the temporal distribution of rainfall. Rainfall is a highly variable process over a wide range of scales, and in space and time. Hence, the investigation of all variations in rainfall and other hydrologic processes is crucial (Nicótina et al. 2008). Simulated rainfall in small scale experiments have been successfully used to understand runoff generation, infiltration and other hydrologic processes (Iserloh et al. 2012). Due to the temporal variation in rainfall, the dry time period between rainfall events can allow depletion of depression storage, alter runoff behavior following the dry time period, and cause reduction in top soil moisture content (Dunkerley 2008). Moreover, soil moisture dynamics and saturation could be determined by the rainfall events which in turn may affect surface ponding and overland flow generation process (Dunkerley 2010). Chu et al. (2014) conducted experimental studies on smooth and rough, lab and field surfaces where both artificial and natural multiple rainfall events were applied. It was found that in conjunction with surface microtopography, rainfall characteristics, soil properties, and initial soil moisture affected infiltration and surface runoff dynamics. It also was found that smooth surfaces were more responsive to the rainfall input on the first rainfall event, while in later events the hydrologic connectivity and surface runoff generation became faster for rough surfaces. It also was demonstrated that the hydrologic control factors varied at

any time with rainfall events. Overall, the spatio-temporal variation of precipitation can be one of the main causes for variability in different hydrologic processes and fundamental to surface and subsurface water budget (Bacchi and Kottegoda 1995).

A fundamental research question is: how exactly do multiple rainfall events alter the hydrologic processes of a given system and what are the inter-relationships of these processes? The objective of this study is to evaluate the effects of multiple rainfall events on both surface and subsurface hydrologic processes using the P2P modeling system. The surface processes include surface ponding, infiltration, surface runoff generation, and hydrologic connectivity, while the subsurface processes involve wetting front movement, and drainage and redistribution. Moreover, the interaction between surface and subsurface hydrologic processes is also examined.

3.3. Materials and Methods

The topographic surface selected for this study was located at the North Dakota State University agricultural research fields. It had a surface area of 179,200 cm^2 (560 × 320 cm) with a grid size of DX = 5 cm (Figure 3.1). The total soil profile was 60-cm deep and for the purpose of subsurface process simulation, it was discretized into 3-mm cells. The original surface was scanned in the field by using an instantaneous-profile laser scanner (Chu et al., 2010). The horizontal and vertical resolutions of the laser scanner were 0.98 and 0.5 mm, respectively. A 5-cm DEM was created by employing the Kriging method.

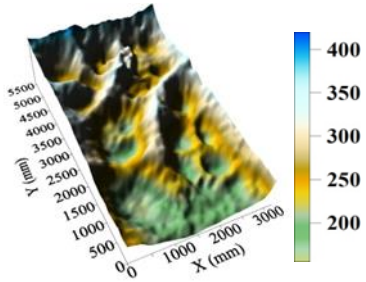

Figure 3.1. DEM surface used for the P2P modeling (DX = 5 cm)

3.3.1. Modeling scenarios

The P2P model (Chu el al. 2013a and b) was used to simulate the impacts of multiple rainfall events on surface and subsurface hydrologic processes. To enable this evaluation, three modeling scenarios (M1, M2, and M3) were considered. The total simulation time periods for M1, M2, and M3 were 200, 270, and 540 min, respectively and a time interval of Δt = 1 min was selected. For all the modeling scenarios, the same topographic surface, soil type (sandy loam), and initial soil moisture content (θ_0) were used. It was assumed that the soil was uniformly distributed across the topographic surface. Thus, only one soil zone was considered in the P2P modeling. Table 3.1 shows the soil hydraulic parameters for the selected soil. A uniform distribution of initial soil moisture (θ_0 = 0.2 cm^3/cm^3) was assumed in the modeling.

Table 3.1. Major soil hydraulic parameters [a]

Parameters	Values
Saturated hydraulic conductivity K_s (cm/h)	4.42
Suction head h_s (cm)	11.01
Saturated water content θ_s (cm^3/cm^3)	0.41
Residual water content θ_r (cm^3/cm^3)	0.065
Soil water retention parameter n	1.89
Soil water retention parameter α (1/cm)	0.075

[a] Carsel and Parrish, 1988.

3.3.2. Rainfall distribution

Three different synthetic multiple rainfall distributions were applied on the selected field plot surface. The first and second rainfall distributions (RF1 and RF2) had two events each (Figures 3.2a and 3.2b), while the third rainfall distribution (RF3) had three events (Figure 3.2c). The three rainfall distributions (RF1, RF2, and RF3) corresponded with the three modeling scenarios (M1, M2, and M3). For the three rainfall distributions, the intensities and durations of

the first event were identical. The first rainfall event was repeated twice for RF1 and RF2, and thrice for RF3 with a dry time period in-between (Figure 3.2).

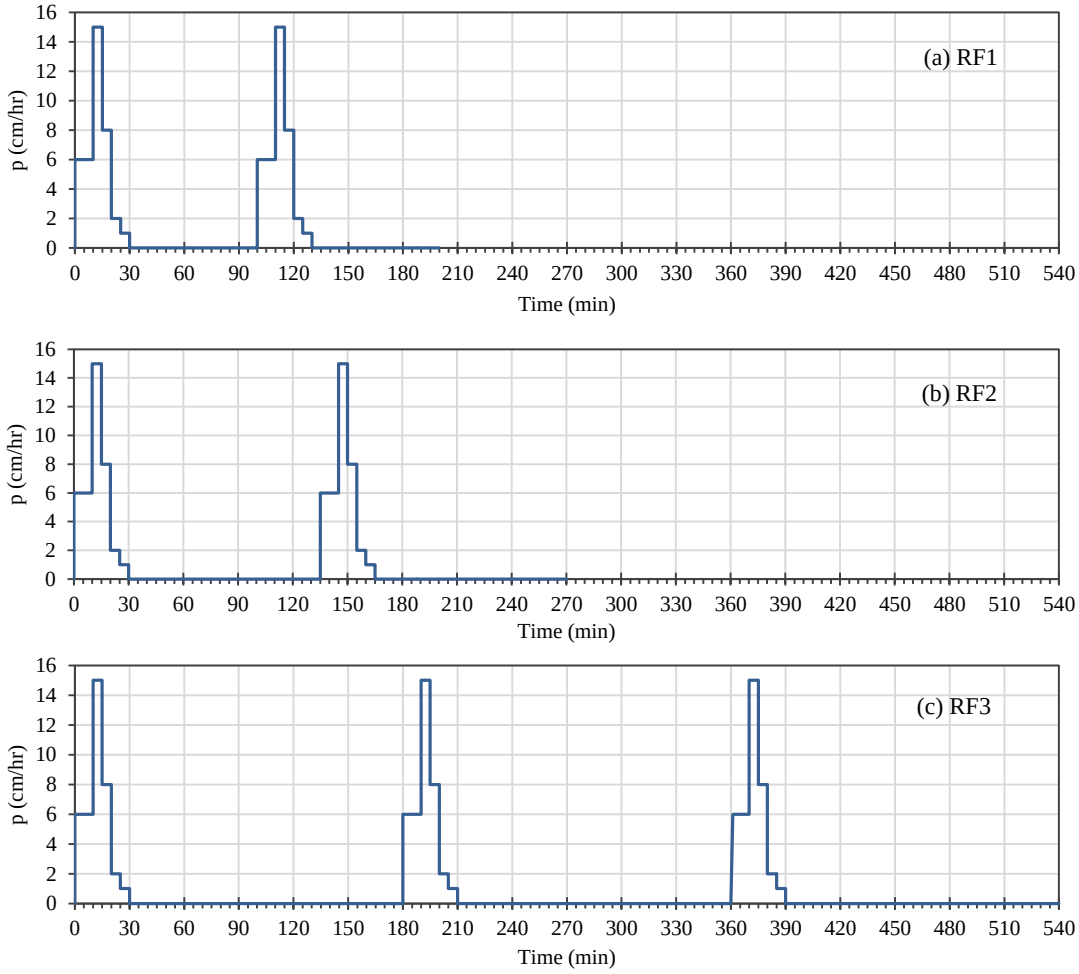

Figure 3.2. Three multiple rainfall distributions (RF1, RF2, and RF3)

The intensities of the first unsteady rainfall event (Figure 3.2) were 6.0 cm/hr at t = 0 - 10 min, 15.0 cm/hr at t = 11 - 15 min, 8.0 cm/hr at t = 16 - 20 min, 2.0 cm/hr at t = 21 - 25 min, and 1.0 cm/hr at t = 26 - 30 min. For the first rainfall distribution (RF1), an identical event was repeated at t = 101 - 130 min and there was no rain during t = 31 - 100 min and t = 131 - 200 min. RF2 (Figure 3.2b) was similar to RF1 except that the modeling time period was extended to allow depletion of ponded water before the beginning of the second event. The first event of RF2

was replicated at t = 136 - 165 min and there was no rain during t = 31 - 135 min and t = 166 - 270 min.

For RF3, the first event was replicated at t = 181 - 210 min and t = 361 - 390 min and there was no rain during t = 31 - 180 min, t = 211 - 360 min and t = 391 - 540 min. For RF3 (Figure 3.2c), the dry time period was extended further to allow enough time for the puddle draining process to take place. After the second event of RF3, the ponded depressions needed a longer time to drain when compared with the draining time needed after the first event. To maintain consistency, the longest dry time period was adopted for all events of RF3. It was assumed that rainfall was uniformly distributed across the soil surface and only one rainfall zone was considered in the P2P modeling.

3.4. Results and Discussions

3.4.1. Effects of multiple rainfall events on subsurface processes

Eight representative cells (C1 - C8) were selected from the topographic surface (Figure 3.3) to analyze soil water dynamics. Seven of them (C2-C8) were located inside a puddle that had 5 levels, while cell C1 was located outside of any puddle. C1 was a non-puddle cell; C2 was in the highest level-5 puddle; C3 and C4 were in the level-4 puddle; C7 and C8 were in the level-3 puddle; and C5 and C6 were in the level-1 puddle.

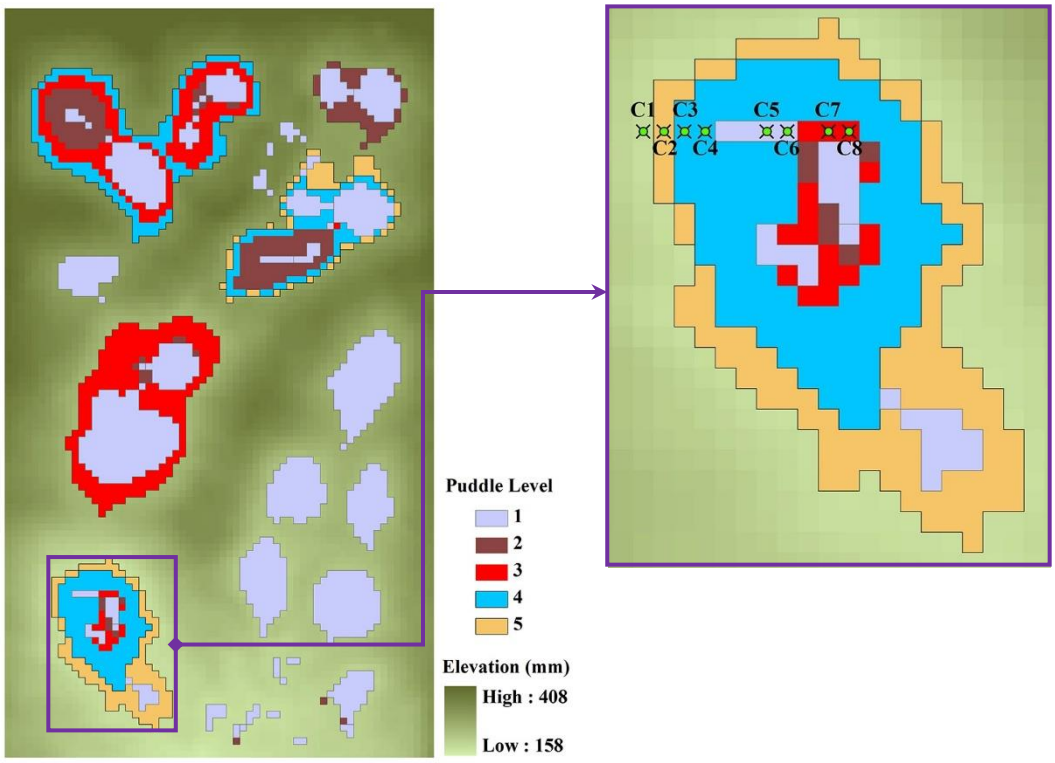

Figure 3.3. DEM grid cells of different puddle levels

Figure 3.4 shows the soil moisture distribution along the soil profile of cell C4 (Figure 3.3) for RF3. Initially, the soil profile had a uniform moisture distribution which was depicted by a vertical line (Figure 3.4). After rainfall started, the top soil became saturated and the moisture content surged immediately, which was represented by a sudden break of the vertical line in the moisture profile curve (Figure 3.4). As rainfall continued, the sharp wetting front moved deeper and more water percolated into the soil profile. After rainfall ceased at t = 30 min, moisture redistribution process was triggered. This was depicted by a curve facing to the left (Figure 3.4). The inflection point of the curve was the dividing line between upward and downward moisture movements. Above this point, water moved upward primarily due to evapotranspiration and below it water drained downward. The inflection point continuously changed its position until upward and downward forces were virtually in equilibrium or interrupted by another rainfall event. The tail of this curve was still vertical as the moisture did not change from its initial value.

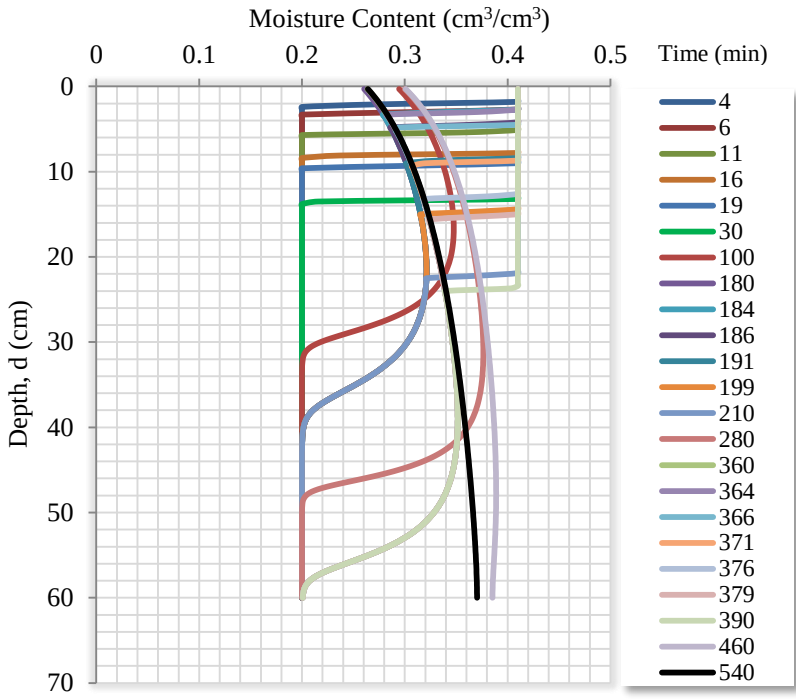

Figure 3.4. Moisture distribution along the soil profile of cell C4 for RF3

Once the second rainfall event started at t = 181 min, the wetting front moved again in a sharp front (Figure 3.4). Moisture augmentation resumed from the previous redistribution stage which had a curved moisture distribution. After the second rainfall event, the moisture curve again exhibited a sharp wetting front (Figure 3.4). After the second rainfall event ended, the second stage of drainage and redistribution took over. At this stage, multiple curvatures were observed in the curve. As the moisture redistribution continued, the two curves merged and the redistribution was represented by a single-curvature curve (Figure 3.4). As the moisture content in the deeper soil increased, the curve became more bulged (Figure 3.4). By the end of the modeling time period (t = 540 min), the initial moisture content of the entire soil profile was changed and reached near saturation.

Figure 3.5 shows the temporal distributions of soil moisture for RF3 at depth of d = 24 cm for cells C1-C8 (Figure 3.3). After the beginning of the first rainfall event, water did not

immediately percolate to this depth which was depicted by a horizontal line at the beginning of the curves for all cells (Figure 3.5). In cell C8, due to the first rainfall event, the sharp moving wetting front was sustained until t = 53 min and reached a depth of 20.1 cm. Right after this time, drainage and redistribution was triggered and a sharp increase of moisture was noticed at d = 24 cm (Figure 3.5). For cell C8, when the moisture content reached 0.348 cm^3/cm^3, it declined to θ = 0.329 cm^3/cm^3 due to drying.

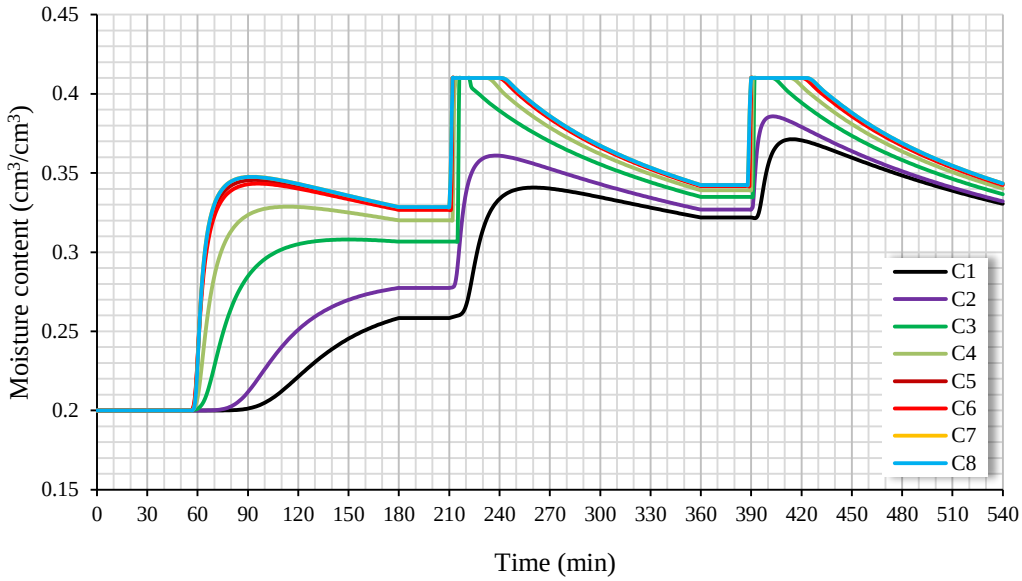

Figure 3.5. Temporal distributions of soil moisture of eight cell profiles for RF3 at depth d = 24 cm

The moisture drainage and redistribution were interrupted by the second rainfall event and once the wetting front reached d = 24 cm, the moisture surged to a saturation value at t = 212 min (cell C8, Figure 3.5). This was also 2 min after the end of the second rainfall event. Saturation was sustained for 30 min (until t = 241 min) in cell C8, after which the second stage of redistribution was triggered. And the moisture declined until it was interrupted by the third rainfall event at t = 360 min (Figure 3.5). Right before the third rainfall event the moisture content in cell C8 was 0.342 cm^3/cm^3. At t = 390 min the soil became fully saturated again as a

result of the third rainfall event. Saturation was maintained for 35 min (until t = 424 min) which was longer than that of the second rainfall event.

After t = 424 min time, the third stage drainage and redistribution was initiated and the moisture content declined. By the end of the modeling time period (t = 540 min) the moisture content in cell C8 was 0.343 cm^3/cm^3. Similar patterns can be observed for other cells (C1 – C7) (Figure 3.5) although the magnitude of the moisture content was smaller. For the non-puddle cell (C1), the wetting front never reached the depth of 24 cm and as a result it was never fully saturated (Figure 3.5). The moisture increase in the soil profile of that cell was due to drainage and redistribution. Moreover, moisture drainage and redistribution for C1 did not take effect until t = 85 min. The temporal distributions of soil moisture for other cells (C2 – C7) were between cells C1 and C8 (Figure 3.5). Overall, the temporal moisture distribution of the eight selected cells (C1-C8) was different and the variations were function of rainfall event. Spatial location of the cells affected, the soil water dynamics. If ever achieved, saturation was only after the first event of RF3.

3.4.2. Effects of multiple rainfall events on infiltration

Prior to the application of the first rainfall event, the surface was basically dry (θ_0 = 0.2 cm^3/cm^3). Figure 3.6 shows the spatial distributions of cumulative infiltration for the two rainfall events of RF2 at a set of critical time steps. The time steps represented the ponding times for the first and second rainfall events (t = 11 min and t = 137 min, respectively) (Figures 3.6a2 and 3.6b1), the ending times of both rain events (t = 30 and 165 min) (Figures 3.6a3 and 3.6b3), typical time steps at a dry time period (t = 85 and 165 min) (Figures 3.6a4 and 3.6b4), and the ending times of the dry periods (t = 135 and 270 min) (Figures 3.6a5 and 3.6b5). To enable

analysis of cumulative infiltration at comparable time intervals, *t* = 2 and 146 min (Figures 3.6a1 and 3.6b2) were added to the set of critical times.

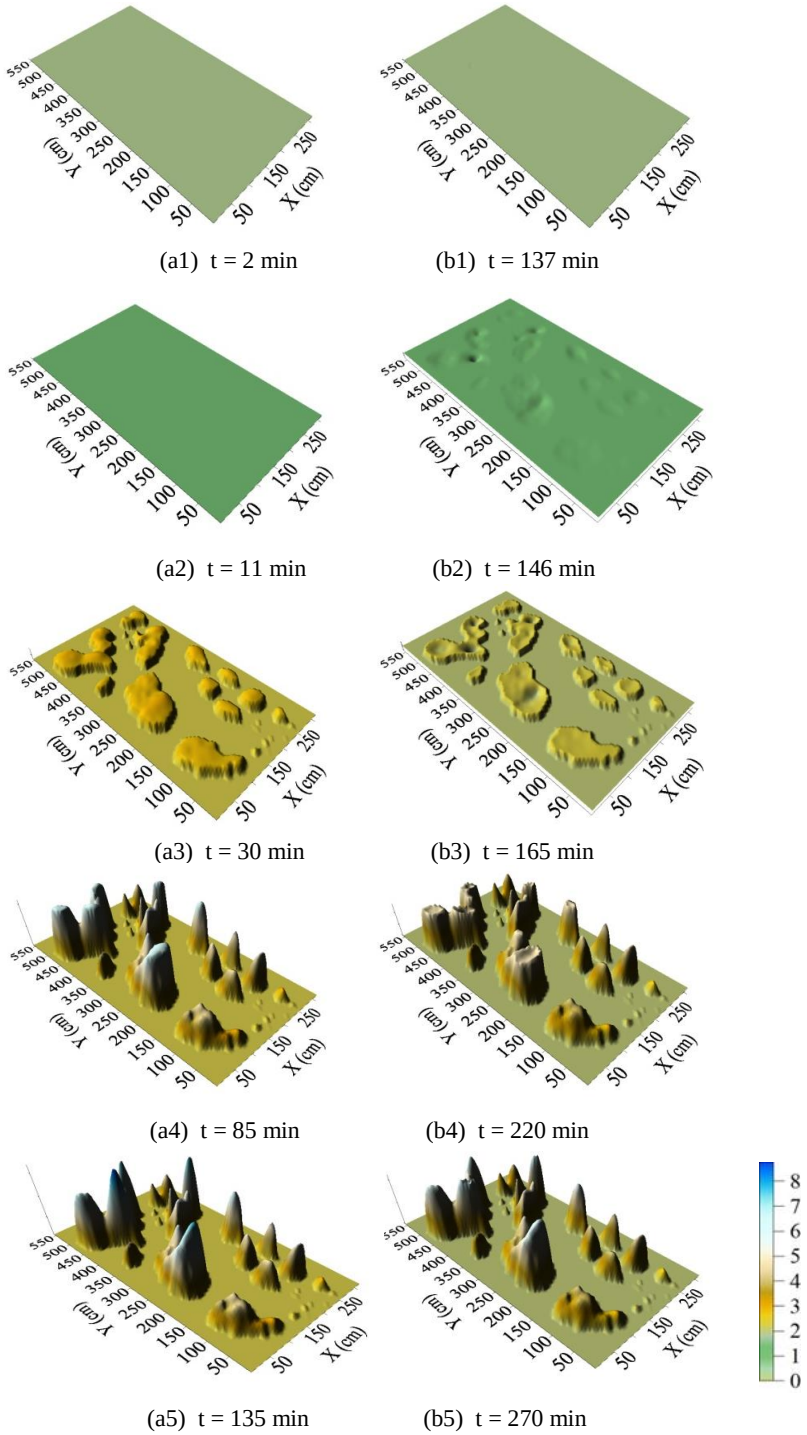

Figure 3.6. Spatial distributions of cumulative infiltration (cm) for RF2

The ranges of cumulative infiltration for the first rainfall event at t = 2, 11, 30, 85, and 135 min were 0 - 0.2 cm, 0 - 1.12 cm, 2.20 - 3.02 cm, 2.20 - 6.44 cm, and 2.20 - 8.76 cm, respectively (Figures 3.6a1 – 3.6a5). The ranges of cumulative infiltration for the second rainfall event at t = 137, 146, 165, 220, and 270 min were 0.18 - 0.20 cm, 0.61 - 1.08 cm, 1.56 - 2.32 cm, 1.97 - 4.84 cm, and 1.97 - 6.49 cm, respectively (Figures 3.6b1 – 3.6b5). The cumulative infiltration in the second rainfall event was lower than that of the first event. This can be attributed to the change in moisture regime of the soil profile as a result of the preceding rainfall event.

After the second rainfall event started at t = 136 min, interesting reversal of the pattern of cumulative infiltration for the non-puddle and puddle cells was observed. In the first event, cumulative infiltration was higher at the puddle center due to the higher ponded water depth and it decreased towards the puddle boundaries, while non-puddle cells had the lowest value. This resulted in spatial and temporal variability in the soil water dynamics across the topographic surface.

The non-puddle cells dried before puddle cells and underwent a process of moisture drainage and redistribution first. Resultantly, in the second event, the infiltration rate was higher in the non-puddle cells than in puddle cells. In the puddles, the boundary cells dried before the central cells. This caused a spatio-temporal variation in soil water dynamic with-in a puddle itself. The pattern of cumulative infiltration resembled the shape of the topographic surface when the puddle filling process was dominant (Figures 3.6a3 and 3.6a4). When the puddle depleting process was triggered, ridges with depressed top (Figures 3.6b3 and 3.6b4) were observed due to the spatial variability of soil moisture movement in boundary and central puddle cells.

For RF1, the spatial distribution of cumulative infiltration at the end of the first dry time period was similar to that at the end of the second dry time period, however, with a smaller magnitude. The cumulative infiltration values at the end of the first and second dry time periods of RF1 were 484,034 and 421,697 cm^3, respectively. This also signified the reduction in cumulative infiltration due to stagnation of water in the depressions as a result of retarded soil water movement. For RF2, everything was similar to that of RF1 except the longer modeling period (270 min) that resulted in more infiltration and depletion of the surface depression storage. The cumulative infiltration values at the end of the first and second dry periods of RF2 were 484,559 cm^3 and 437,545 cm^3, respectively.

For RF3, the distribution of cumulative infiltration was similar to that of RF2. The first rainfall event of RF3 had a similar pattern to the corresponding event of RF2 while the second and third events of RF3 showed a behavior similar to that of the second event of RF2. The cumulative infiltration values at the end of first, second, and third dry time periods at t= 180, 360, and 540 min were 484,559 cm^3, 447,610 cm^3, and 443,057 cm^3, respectively. This signified a considerable reduction of cumulative infiltration as the number of rainfall events increased. The analyses of the results for the three rainfall events of RF3 suggested that infiltration decreased with the occurrence of more rainfall events. Moreover, the prevalence of depressions caused a variation of hydrologic response to different rainfall events. Resultantly, cumulative infiltration distributions varied across the spatial domain.

3.4.3. Effects of multiple rainfall events on surface depression storage

Figure 3.7 shows the ponded water distributions for the two rainfall events of RF2 at critical time steps (t = 2, 11, 30, 85, 135, 137, 146, 165, 220, and 270 min). When ponding condition was achieved at t = 137 min in the second rainfall event (2 min after the start of the

second event), infiltration was still the dominant process in the first event (t = 2 min) and water did not start to accumulate on the surface yet. When ponding condition was achieved in the first event at t = 11 min, 29,842 cm^3 of water was already ponded on the surface at the corresponding time step of the second event (t = 146 min). The time of, t = 146 min was 11 min after the start of the second rainfall event. By the end of the first (t= 30 min) and second (t = 165 min) events, 63,033 cm^3 and 71,755 cm^3 of water were accumulated in the surface depressions, respectively. In the dry time period of the first and second events of RF2, the ponded water volume declined and at t = 85 and 220 min the volume reached 2,248 cm^3 and 6,690 cm^3, respectively. By the end of the first (t= 135 min) and second (t = 270 min) dry time periods, 0 cm^3 and 190 cm^3 of water were accumulated in the surface depressions, respectively. The depression storage dynamics was different for all the events of the multiple rainfall distributions (RF1 – RF3). Both ponding time and the time to attain MDS were affected by the temporal distribution of the rainfall events.

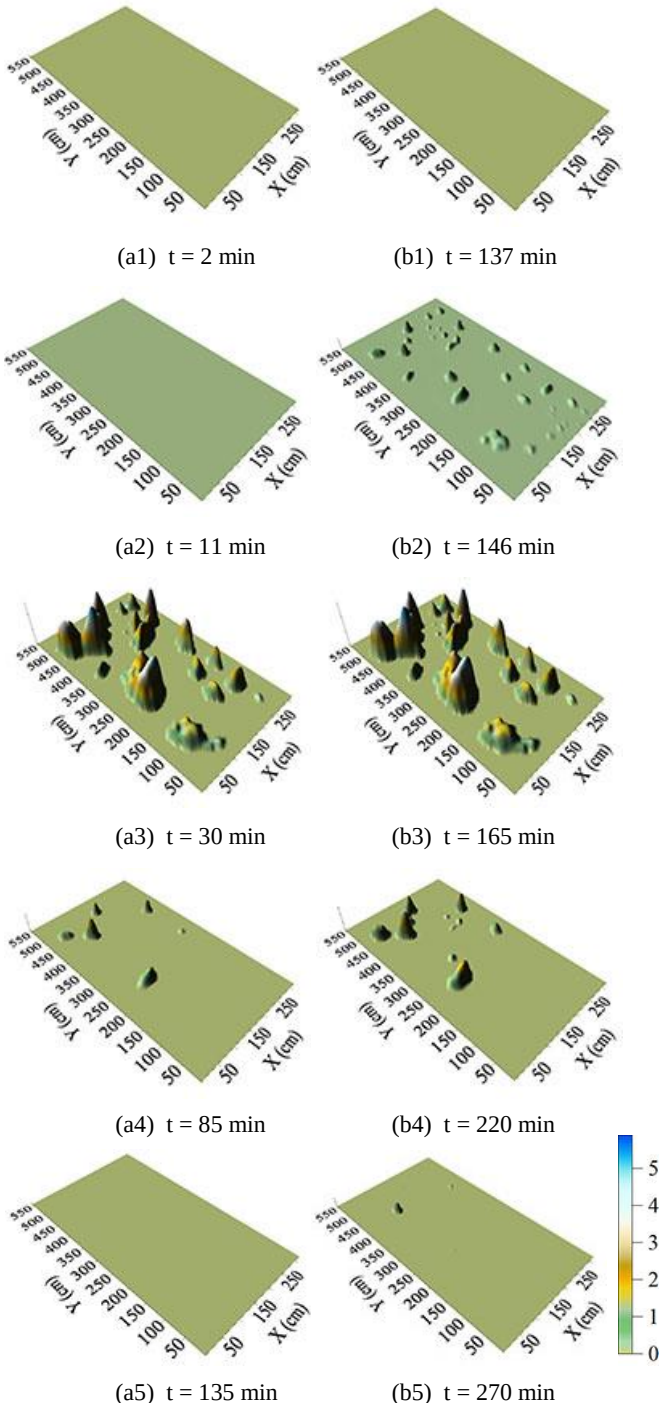

Figure 3.7. Spatial distributions of ponded water depths (cm) for RF2

For the first rainfall event of RF1, the ponding time and the time to reach MDS were longer than the corresponding times for the second rainfall event. The ponding condition in the second event of RF1 was achieved instantly (t = 101 min) while MDS was reached at t = 115

min which was 4 min earlier than in first event of RF1. This can be attributed to the increase in the initial moisture content of the soil in the dry cells and saturation of the upper soil layer in water-ponded cells, both of which were due to the previous rainfall event. Water level in the puddles increased quickly during the second rainfall event. However, once MDS was reached the spatial distribution of the ponded water was identical for both events. Once rainfall stopped, the puddle levels started to decrease and the rate of depletion was found to be different in both events. Due to the change in the initial moisture condition in the soil profile in the second event, the puddle draining process was slower than the first event. At the end of the second dry time period, there was 2,708 cm^3 of ponded water while it was only 535 cm^3 at the end of the first dry period.

For RF2, the ponding time and the time to reach MDS in the first event were identical to those of the first event of RF1 (t = 11 and 19 min, respectively) (Figure 3.7). The ponding time (t = 137 min) and the time to reach MDS (t = 150 min) in the second rainfall event were 9 and 4 min shorter than those in the first rainfall event, respectively. As there was no ponded water before the beginning of the second rainfall event of RF2 (Figure 3.7a5), the ponding time was delayed by 2 min when compared with second event of RF1, although MDS was reached simultaneously. The puddle depleting process was faster in the first dry time period of RF2 than in the second dry time period of RF2. At the end of the first and second dry time periods of RF2, surface depression storages were 0 cm^3 and 190 cm^3, respectively.

For RF3, the ponding time and the time to reach MDS for the first event were identical to those of the first event of RF1 and RF2 (t = 11 and 19 min, respectively). In the second event, ponding condition and MDS were achieved at t = 186 and 196 min, respectively, while for the third event they were attained at t = 364 and 376 min. The ponding time of the second rainfall

event was 5 min shorter than that of the first event and for the third rainfall event it was 7 min shorter than that of the first event. The time to reach MDS was equal for the second and third rainfall events (t = 16 min), which was 3 min shorter than that of the first rainfall event. At the end of the dry time periods of all rainfall events of RF3, all surface depressions were empty. The time to reach MDS was the same for the second and third rainfall events although they reached the ponding condition at different times. This can be attributed to the P2P filling-spilling-merging-splitting dynamic process. That means, although the time to reach MDS was the same for the second and third events of RF3, the implication of the third rainfall event can be reflected indirectly in other hydrologic processes such as increased outlet discharge.

3.4.4. Effects of multiple rainfall events on hydrologic connectivity

Figure 3.8a shows the temporal distributions of the numbers of connected areas for the three rainfall events of RF3. The effect of temporal rainfall distribution was less pronounced in the wet time periods. However, in the dry time periods the differences were very discernible. This can be attributed to the reduction in the rate of infiltration as a result of saturation of the upper soil zone from the subsequent rainfall events. And consequently, puddle filling and merging processes were quicker in the second and third events while puddle splitting process was relatively slower in the later dry time periods when compared to the first event of RF3. Moreover, MDS was sustained for a longer time period in later rainfall events. The increase in moisture content reduced the ponding time and infiltration rate thereby enhanced the hydrologic connectivity. In addition, the relationship of rainfall intensity, duration, and event is important when analyzing the dynamics of hydrologic connectivity as it may be facilitated or delayed, depending on the pattern of rainfall.

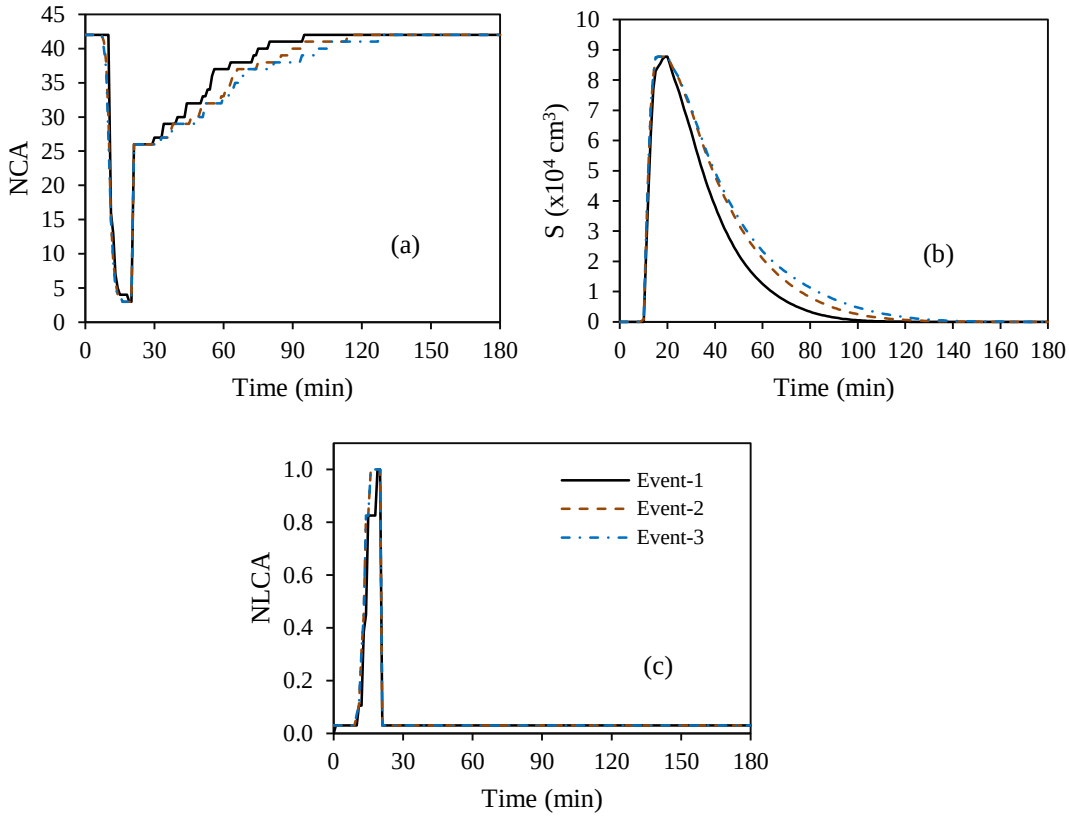

Figure 3.8. (a) Number of connected areas (NCA), (b) depression storage (S), and (c) normalized connected area to the outlet (NLCA) for RF3

Figure 3.8b shows the depression storage of the topographic surface. This increased constantly when P2P process was underway and it peaked 19 min after the start of the first event and 16 min after the start of the second and third events. After sustaining MDS for 2 min in the first event and 5 min in the second and third events, the depression storage declined and ultimately it became zero by the end of each dry time periods. It must also be noted that although the three events happened in series they were overlapped in one figure (Figure 3.8b) for the ease of comparison. For the second and third events, the depression storage curves were receding gently, while for the first event this curve was receding sharply showing a faster storage depletion rate.

Figure 3.8c shows the temporal variations in normalized connected area to the outlet (NLCA). NLCA is the ratio of the area that is hydrologically connected to the outlet to the total area. The horizontal portion at the beginning of the curves shows the time before ponding condition was reached and the area that was structurally connected the outlet. After the ponding time, NLCA increased continuously. When MDS was reached, NLCA reached its maximum value of 1. Then after the rainfall intensity decreased, it declined to the initial value. An early maturity of the hydrologic connectivity was noticed in the later rainfall events when compared with the first event.

Hydrologic connectivity was one of the variables that were affected by the temporal distribution of rainfall. When the topographic surface was dry, the hydrologic connectivity was characterized by structural hydrologic connectivity. The hydrologic connectivity dynamics was a function of rainfall events. In the earlier rainfall event, it took a longer time for the surface to attain full hydrologic connectivity, while in the following rainfall events, hydrologic connectivity was faster. In the dry time period, the separation of connected areas took longer time after the later rain events.

3.4.5. Effects of multiple rainfall events on surface runoff generation

The changes in infiltration, soil water dynamics, and hydrologic connectivity that were resulted from the temporal changes in rainfall affected the way surface runoff was generated. Figure 3.9a shows the surface runoff rate for the three events of RF3. For ease of visualization, only the first 50-min surface runoff rate graphs were shown instead of the whole period of each event (180 min). The runoff initiation times for events one, two, and three of RF3 were 11, 10, and 9 min, respectively. This was attributed to the spatio-temporal change in surface depression storage and subsurface water dynamics as a result of increase in rainfall events. As more rainfall

events occurred, the depression filling time shortened and moisture content of the soil profile increased. Moreover, the limited infiltration capacity of the soil and enhancement in the hydrologic connectivity caused an earlier runoff generation in the later rainfall events. The runoff generation rate was consistent with the non-uniform rainfall events. The peak discharges for rainfall events one, two, and three were 1.30×10^6, 1.53×10^6 and 1.55×10^6 cm^3/hr, respectively. This increase in peak discharge was another effect of multiple rainfall input. The combined effect of spatio-temporal changes in surface and subsurface water dynamics resulted in higher surface runoff and peak discharge.

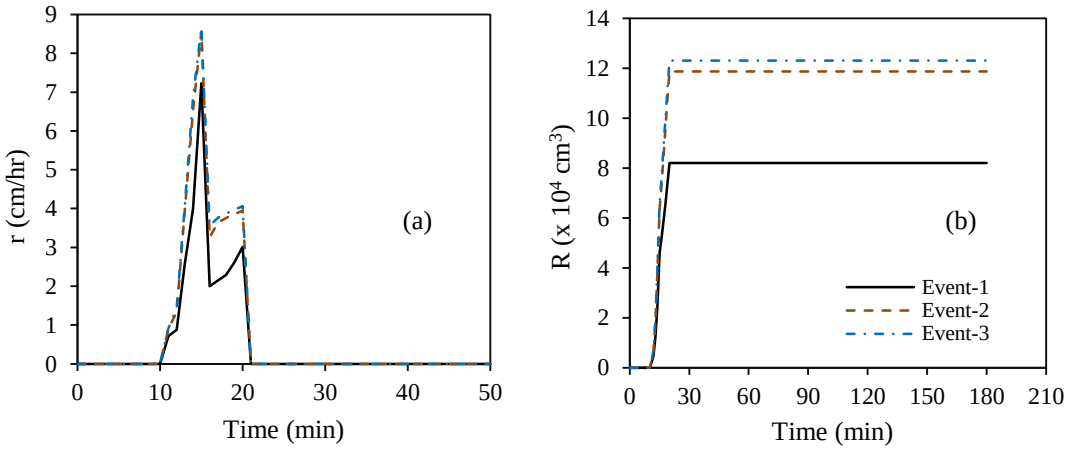

Figure 3.9. (a) Surface runoff rate (r) and (b) cumulative runoff volume (R)

Figure 3.9b shows the cumulative runoff volumes for the three rainfall events of RF3. At the beginning of the first rainfall event, the topographic surface was dry and it had to reach ponding condition before the area connected to the outlet started to contribute runoff or until the P2P filling-spilling-merging-splitting dynamic process was initiated. Cumulative runoff volume increased continuously during the P2P process. Moreover, decrease in cumulative infiltration and the increase in hydrologic connectivity during the later stages of the dynamic P2P process caused an increase in cumulative runoff volume. At the end of the first, second, and third events of RF3, the cumulative runoff volumes were 82,002, 118,610, and 123,007 cm^3, respectively. This can be

attributed to the mutual effects of surface and subsurface hydrologic processes in response to multiple rainfall inputs. The difference in cumulative runoff volumes between the first and second events was more significant than between the second and third events. This can attributed to the reduction in moisture deficit of the soil profile with occurrence of more rainfall events

3.5. Summary and Conclusions

In this study, the effects of temporal distribution of rainfall on hydrologic processes were analyzed and evaluated. To enable this evaluation, three modeling scenarios that corresponded to three different types of multiple rainfall distributions were created and analyzed using the P2P modeling system. From the modeling results, it was found that temporal rainfall distribution affected many hydrologic processes. In the first event of all the scenarios, the behaviors of all hydrologic processes investigated were identical as there was no rainfall prior to this event. A pronounced variation in the hydrologic processes was observed in the second and third rainfall events. Temporal variations in rainfall caused corresponding spatial and temporal changes in the soil water dynamics. The wetting front moved deeper as more rainfall was precipitating on the surface and the moisture content in the deeper soil was boosted via drainage and redistribution; and how deep this redistribution goes was function of the wetting front depth prior to the drainage and redistribution. The ponding time and the time to reach maximum depression storage (MDS) were generally shorter in the later rainfall events. This caused spatial variability of surface water ponding. Due to the slower puddle depleting process and variation in the sustainability of surface water ponding, spatial variations in soil moisture content were observed. This in turn affected the spatial distribution of infiltration. Hydrologic connectivity was enhanced as a result of earlier saturation of the top soil and reduction of infiltration. The

reduction in ponding time and infiltration, and the enhancement of hydrologic connectivity in turn caused earlier and greater surface runoff generation.

3.6. References

Bacchi, B., and Kottegoda, N. T. (1995). "Identification and calibration of spatial correlation patterns of rainfall." *Journal of Hydrology*, 165, 311–348.

Carsel, R. F., and Parrish, R. S. (1988). "Developing joint probability distributions of soil water retention characteristics." *Water Resources Research,* 24(5), 755–769.

Chu, X., Padmanabhan, G., and Bogart, D. (2014). "Microrelief-controlled overland flow generation: laboratory and field experiments." *Transactions of the ASABE,* under review.

Chu, X., Yang, J., Chi, Y., and Zhang, J. (2013a). "Dynamic puddle delineation and modeling of puddle-to-puddle filling-spilling-merging-splitting overland flow processes." *Water Resources Research*, 49(6), 3825–3829.

Chu, X., Zhang, J., Yang, J., Habtezion, N., Chi, Y., and Yang, Y. (2013b). *P2P Modeling System, User's Manual*, Version 1.50, North Dakota State University.

Chu, X., Zhang, J., Chi, Y., and Yang, J. (2010). "An improved method for watershed delineation and computation of surface depression storage", p1113-1122. In: Watershed Management 2010: Innovations in Watershed Management Under Land Use and Climate Change, Proceedings of the 2010 Watershed Management Conference, edited by K. W. Potter and D. K. Frevert. American Society of Civil Engineers.

Dunkerley, D. (2008). "Rain event properties in nature and in rainfall simulation experiments: a comparative review with recommendations for increasingly systematic study and reporting." *Hydrological Processes,* 22, 4415–4435.

Dunkerley, D. L. (2010). “How do the rain rates of sub-event intervals such as the maximum 5- and 15-min rates (I_5 or I_{30}) relate to the properties of the enclosing rainfall event?” *Hydrological Processes*, 22, 2425–2439.

Iserloh, T., Fister, W., Seeger, M., Willger, H., and Ries, J. B. (2012). “A small portable rainfall simulator for reproducible experiments on soil erosion.” *Soil & Tillage Research*, 124, 131–137.

Nicótina, L., Celegon, A. E., Rinaldo, A., and Marani, M. (2008). “On the impact of rainfall patterns on the hydrologic response.” *Water Resources Research*, 44, W12401.

CHAPTER 4. OVERALL CONCLUSIONS AND FUTURE WORK

This thesis research addressed (1) the effects of DEM resolution on microtopographic characteristics, hydrologic connectivity, and modeling of hydrologic processes; and (2) the influences of multiple rainfall events on surface and subsurface hydrologic processes with the use of the P2P modeling system for different scenarios.

In Chapter 1, a brief overview of surface microtopography and the associated factors that affect hydrologic modeling, and an introduction to the P2P modeling system were given. In addition, DEM- and image-based approaches that had been used for topographic characterization were introduced. The P2P model is a quasi-3D, distributed model that simulates overland flow across a topographic surface as well as infiltration and unsaturated flow in heterogeneous soils under complex rainfall events that may include both wet and dry time periods. The novel features of the P2P modeling system enable a unique analysis of hydrologic processes. The P2P model also encompasses a series of tools that can be used independently for surface microtopography characterization and analysis. Object-based image segmentation (OBIS) is one of the P2P tools, which implements object-based image analysis (OBIA) to partition images to a desired number of clusters. The surface topographic parameter tool (STP) is used to calculate and visualize slope, aspect, and different types of curvature. The puddle delineation (PD) tool is a part of the P2P model for identification of puddle cells, centers, thresholds, flats, and their levels, computation of maximum depression storage (MDS) and maximum ponding area (MPA), and determination of the relationships of multiple puddles. The results of the PD program are used in modeling of the dynamic P2P processes.

In Chapter 2, the effects of DEM resolution on microtopographic characteristics, hydrologic connectivity, and modeling of hydrologic processes were studied. Specifically, this

chapter covered the spatial and temporal changes in hydrologic connectivity, surface depression storage, and infiltration as DEM resolution changed. The effects of DEM resolution on surface runoff and MDS were also discussed. Analysis of several microtopographic characteristics was included and the chapter as a whole described the interrelationships of surface microtopographic characteristics, hydrologic connectivity, and various hydrologic processes. Nine modeling scenarios corresponding to different DEM resolutions were created to evaluate their impacts.

The change in DEM resolution had a significant effect on how surface microtopography was depicted. Full representation of the natural heterogeneity of a topographic surface was not possible as a result of the smoothing and aggregation effect induced by increasing DEM grid size, which tended to eliminate important topographic features. DEM grid size affected both structural and functional hydrologic connectivity. Reduction in DEM resolution tended to "enhance" hydrologic connectivity and resulted in early maturity of functional hydrologic connectivity. In contrast, a higher resolution DEM captured more detailed topographic features and the relevant surface was subject to smaller-scale dynamic processes before it reached a fully-connected status. Coarser resolution DEMs exhibited the propensity to mask the effect of important land surface features, ultimately creating a surface that consisted of a number of large planar DEM grids and resulting in virtually highly connected areas. During a rainfall event, the topographic surface became more responsive to connectivity.

The change in DEM resolution altered hydrologic processes simulated by the P2P model. As the DEM grid size became larger, the topographic heterogeneity and roughness of a natural surface were reduced and the filling time of depressions was shortened, which in turn caused higher outlet discharge at earlier stages of a rainfall period. Surface ponded water depth decreased with an increase in DEM grid size. The spatial distribution of ponded water depths

strongly depended on DEM grid size. The influence of DEM resolution on infiltration mainly occurred after rainfall stopped. The spatial distribution of cumulative infiltration was strongly affected by DEM resolution, which was primarily associated with puddles and their distributions. The greater MDS of a higher resolution surface sustained infiltration for a prolonged period of time, maintained higher soil moisture content, and yielded a deeper wetting front.

In Chapter 3, the effects of temporal distribution of rainfall on the surface and subsurface hydrologic processes were simulated and evaluated. The changes in spatio-temporal distributions of infiltration and surface depression storage, and wetting front movement that were induced by different rainfall events were discussed. Moreover, this chapter also covered the effects of multiple rainfall events on hydrologic connectivity, depression filling time, and the time to reach maximum depression storage. Three multiple rainfall distributions were created to quantify and underline their effects on different hydrologic processes. The first rainfall distribution had two rain events with ponded water on the surface before the beginning of the second event. The second rainfall distribution was similar to the first event except that the modeling time period was increased to allow full drainage of the ponded water from the first rainfall event. The third rainfall distribution had three rain events and there was no ponded water before the start of the subsequent rainfall events.

From the P2P simulation results, it was found that temporal rainfall distribution affected both surface and subsurface hydrologic processes and the system responded differently to each rainfall event. In the first event of all the scenarios, the behaviors of all hydrologic processes investigated were identical as there was no rainfall prior to this event. A pronounced variation in the hydrologic processes was observed in the second and third rainfall events. Temporal variations in rainfall caused corresponding spatial and temporal changes in the soil water

dynamics. The wetting front moved deeper as more rainfall was precipitating on the surface and the moisture content in the deeper soil was boosted via drainage and redistribution. How deep the redistribution goes was a function of the wetting front depth prior to the drainage and redistribution. The ponding time and the time to reach maximum depression storage (MDS) were generally shorter in the later rainfall events. This caused spatial variability of surface water ponding. Due to the slower puddle depleting process and variation in the sustainability of surface water ponding, spatial variations in soil moisture content were observed. This in turn affected the spatial distribution of infiltration. Hydrologic connectivity was enhanced as a result of moisture augmentation and reduction of infiltration. The reduction in ponding time and infiltration, and the enhancement of hydrologic connectivity further caused earlier and greater surface runoff generation.

As described earlier, this thesis research had very specific goals and, in this regard, the effects of DEM resolution on hydrologic processes were addressed using a field plot surface where the originally scanned data was used to create different DEM resolution surfaces. Moreover, the field plot surface was used to address the effects of multiple rainfall events on hydrologic processes. For future research, the number of scenarios can be increased by using different topographic surfaces that may include rough and smooth surfaces, in field and/or lab setups; the soil types used and their homogeneity can be varied; the distribution of rainfall and soil can be varied spatially instead of using uniform distribution only. The P2P model has the capability to handle all such combinations and the addition of more scenarios can allow the coverage of a wide range of hydrologic topics.